

## Spatially Resolved Circumgalactic Medium Around a Star-Forming Galaxy Driving a Galactic Outflow at $z \approx 0.8$

AHMED SHABAN <sup>1</sup>, RONGMON BORDOLOI <sup>1</sup>, JOHN M. O'MEARA <sup>2</sup>, KEREN SHARON <sup>3</sup>, NICOLAS TEJOS <sup>4</sup>,  
SEBASTIAN LOPEZ <sup>5</sup>, CÉDRIC LEDOUX <sup>6</sup>, L. FELIPE BARRIENTOS <sup>7</sup>, AND JANE R. RIGBY <sup>8</sup>

<sup>1</sup>*Department of Physics, North Carolina State University, Raleigh, NC 27695-8202, USA*

<sup>2</sup>*W. M. Keck Observatory, 65-1120 Mamalahoa Hwy, Kamuela, HI 96743, USA*

<sup>3</sup>*Department of Astronomy, University of Michigan, 1085 South University Ave, Ann Arbor, MI 48109, USA*

<sup>4</sup>*Instituto de Física, Pontificia Universidad Católica de Valparaíso, Casilla, 4059 Valparaíso, Chile*

<sup>5</sup>*Departamento de Astronomía, Universidad de Chile, Casilla 36-D, Santiago, Chile*

<sup>6</sup>*European Southern Observatory, Alonso de Córdova, 3107 Vitacura, Casilla 19001, Santiago, Chile*

<sup>7</sup>*Instituto de Astrofísica, Pontificia Universidad Católica de Chile, Av. Vicuña Mackenna 4860, 7820436, Macul Santiago, Chile*

<sup>8</sup>*Astrophysics Science Division, Code 660, NASA Goddard Space Flight Center, 8800 Greenbelt Rd., Greenbelt, MD 20771, USA*

### ABSTRACT

We report the small-scale spatial variation in cool ( $T \sim 10^4 K$ ) Mg II absorption detected in the circumgalactic medium (CGM) of a star-forming galaxy at  $z \approx 0.8$ . The CGM of this galaxy is probed by a spatially extended bright background gravitationally lensed arc at  $z = 2.76$ . The background arc continuously samples the CGM of the foreground galaxy at a range of impact parameters between 54-66 kpc. The Mg II absorption strengths vary by more than a factor of two within these ranges. A power-law fit to the fractional variation of absorption strengths yields a coherence length of 2.7 kpc within these absorption lines. This suggests a high degree of spatial coherence in the CGM of this galaxy. The host galaxy is driving a strong galactic outflow with a mean outflow velocity  $\approx -179$  km s<sup>-1</sup> and mass outflow rate  $\dot{M}_{out} \geq 64^{+31}_{-27}$  traced by blueshifted Mg II and Fe II absorption lines. The galaxy itself has a spatially extended emission halo with a maximum spatial extent of  $\approx 33$  kpc traced by [O II], [O III] and H $\beta$  emission lines. The extended emission halo shows kinematic signatures of co-rotating halo-gas with solar metallicity. Taken together, these observations suggest evidence of a baryon cycle that is recycling the outflowing gas to form the next generation of stars.

*Keywords:* Galaxy Evolution – Circumgalactic Medium – Strong Gravitational Lensing

### 1. INTRODUCTION

The circumgalactic medium (CGM) around galaxies has emerged as a reservoir of baryons and metals across cosmic time (Chen et al. 2010; Rudie et al. 2012; Bordoloi et al. 2014b; Peebles et al. 2014; Werk et al. 2014; Péroux & Howk 2020; Lehner et al. 2022; Bordoloi et al. 2024). The CGM plays an important role in regulating the growth in stellar mass and quenching of star-formation in galaxies (Tumlinson et al. 2017). The chemical enrichment of the CGM can occur via metal-enriched outflows from galaxies, which also provide energy to heat the CGM, thereby playing a major role

in galaxy evolution (Somerville & Davé 2015; Vogelsberger et al. 2020; Faucher-Giguère & Oh 2023; Thompson & Heckman 2024). Without galactic outflows, modern galaxy evolution models fail to reproduce the observed population of galaxies (Oppenheimer & Davé 2006; Somerville et al. 2008; Vogelsberger et al. 2014; Schaye et al. 2015; Hopkins et al. 2014; Somerville & Davé 2015; Naab & Ostriker 2017; Pillepich et al. 2018; Faucher-Giguère & Oh 2023).

Observations have shown that in star-forming galaxies, galactic outflows are ubiquitous across cosmic time (Heckman et al. 2000; Veilleux et al. 2005; Rubin et al. 2010b; Chen et al. 2010; Rubin et al. 2014; Bordoloi et al. 2014b; Heckman et al. 2015; Chisholm et al. 2015, 2016; Rupke 2018; Fox et al. 2019; Veilleux et al. 2020; Xu et al. 2022; Clark et al. 2022; Keerthi Vasani et al. 2023;

Xu et al. 2023). These outflows are multiphased, consisting of ionized, neutral, and molecular gas (Strickland & Heckman 2009; Thompson et al. 2016; Fluetsch et al. 2021; Reichardt Chu et al. 2022). The outflows play a key role in chemical enrichment of the CGM by transporting enriched gas out of the galaxy (Muratov et al. 2017; Hafen et al. 2019), setting the mass-metallicity relation (Tremonti et al. 2004; Ma et al. 2016) and regulating and quenching star-formation in galaxies (Hopkins et al. 2010, 2012; Spilker et al. 2019).

The CGM gas is typically very diffuse, which makes it very hard to detect it in emission. Therefore, it is more common to study the CGM in absorption in the spectra of bright background sources, like quasars (QSO) or galaxies, with some impact parameter from the host galaxy (Bordoloi et al. 2011; Rubin et al. 2010a; Bielby et al. 2019). The lack of a large number of bright background sources typically restricts such studies of statistical analysis of the CGM. To constrain the structure and cohesion of the CGM, we need to probe the CGM at multiple sightlines. However, having more than one QSO sightline probing a CGM is rare.

Recently, the introduction of wide-field integral field unit (IFU) spectrographs in 10-m-class telescopes, combined with gravitationally lensed galaxies or quasars, has made it increasingly possible to probe the CGM of a single foreground galaxy along multiple sightlines (Lopez et al. 2018; Rubin et al. 2018; Bordoloi et al. 2016, 2022; Shaban et al. 2023; Afrumi et al. 2023; Dutta et al. 2024).

In addition, these IFUs have allowed us to map the diffuse emission of the CGM gas or the densest part of the outflow gas in the CGM (Rupke et al. 2019; Burchett et al. 2021; Zabl et al. 2021; Shaban et al. 2022; Leclercq et al. 2022; Dutta et al. 2023; Keerthi Vasan G. et al. 2024; Kusakabe et al. 2024; Perrotta et al. 2024). These pioneering efforts have opened up a new avenue of studying the CGM simultaneously in absorption and emission in a spatially resolved manner.

In this paper, we demonstrate this unique capability and simultaneously map the extended CGM around a  $z \approx 0.8$  galaxy both in absorption and emission. We use IFU observations of a spatially extended gravitationally lensed arc at  $z \approx 2.8$ , which serves as a spatially extended background source; and the cool CGM gas around the  $z \approx 0.8$  galaxy is detected in the spectra of the lensed arc. The IFU observations of the galaxy also show spatially extended emission illuminating the dense CGM, allowing us to map the metallicity and kinematics of that gas.

The paper is organized as follows, in §2, we present the IFU and photometric observations of this field of view.

§3 presents the methods for extracting and modeling the spectra and the spectral energy distribution (SED). We present the results of our analysis and discuss the implications of these results on the CGM properties and compare with literature in §4. We summarize our conclusions in §5. We assume a  $\Lambda$ CDM cosmology with  $H_0 = 70 \text{ km s}^{-1} \text{ Mpc}^{-1}$  and  $\Omega_m = 0.3$ . All the reported magnitudes are AB magnitude values.

## 2. OBSERVATIONS

SGAS J152745.1+065219 is a gravitationally lensed galaxy at  $z \approx 2.76$  which is distorted to an  $6''$  extended arc. The strong gravitational lensing is caused by a foreground galaxy cluster at  $z \approx 0.392$  (Koester et al. 2010). This arc was discovered as part of the Magellan Evolution of Galaxies Spectroscopic and Ultraviolet Reference Atlas (MegaSaura) (Rigby et al. 2018a,b). Figure 1 shows the field of view of this system. In the foreground of this arc, a galaxy is found at  $z = 0.785273 \pm 0.000001$  with an angular separation of  $\approx 8''$  (Figure 2, cyan square), which is the subject of this study. Throughout this paper, we refer to it as galaxy G1. The background arc provides several intervening lines of sight probing the CGM of the galaxy G1 over 54-66 kpc scales. In the following subsections, we describe the different observations obtained in this field to study the CGM of G1. An interloping foreground galaxy is detected 2 arcseconds east of G1. We extract a spectrum for this galaxy and measure its redshift to be  $z_{\text{interloping}} = 0.43084 \pm 0.00001$ . Since it is not associated with G1, we will ignore this galaxy for the remainder of the analysis. In addition, two galaxies G2 and G3 with redshifts  $z_{G2} = 0.78494 \pm 0.00001$  and  $z_{G3} = 0.78542 \pm 0.00001$  to the north-west direction of G1 are detected (Figure 1). These galaxies are at a separation of 235.7 kpc (G2) and 205.5 kpc (G3) from G1, respectively. G2 and G3 have an average impact parameter from the background arc of 248 kpc and 250 kpc, respectively. All three galaxies G1, G2 and G3 exhibit prominent emission in [O II], H $\beta$ , and [O III] transitions. Continuum is detected only for G1, where prominent absorption features (e.g., Mg II and Fe II resonant absorption) are detected (see § 3.1). The stellar masses of G2 and G3 are estimated to be  $\log(M_*/M_\odot) = 10.07^{+0.12}_{-0.12}$  and  $9.17^{+0.18}_{-0.15}$ , respectively, after performing SED fits to the broad band photometry from HST-WFC3 observations of G2 and G3 galaxies (see § 3.3). Since G2 and G3 are at very high impact parameter to the background arc relative to G1, we will not consider them for the rest of the analysis. We report their position and properties here for completeness.

### 2.1. KCWI and MUSE IFU Observations

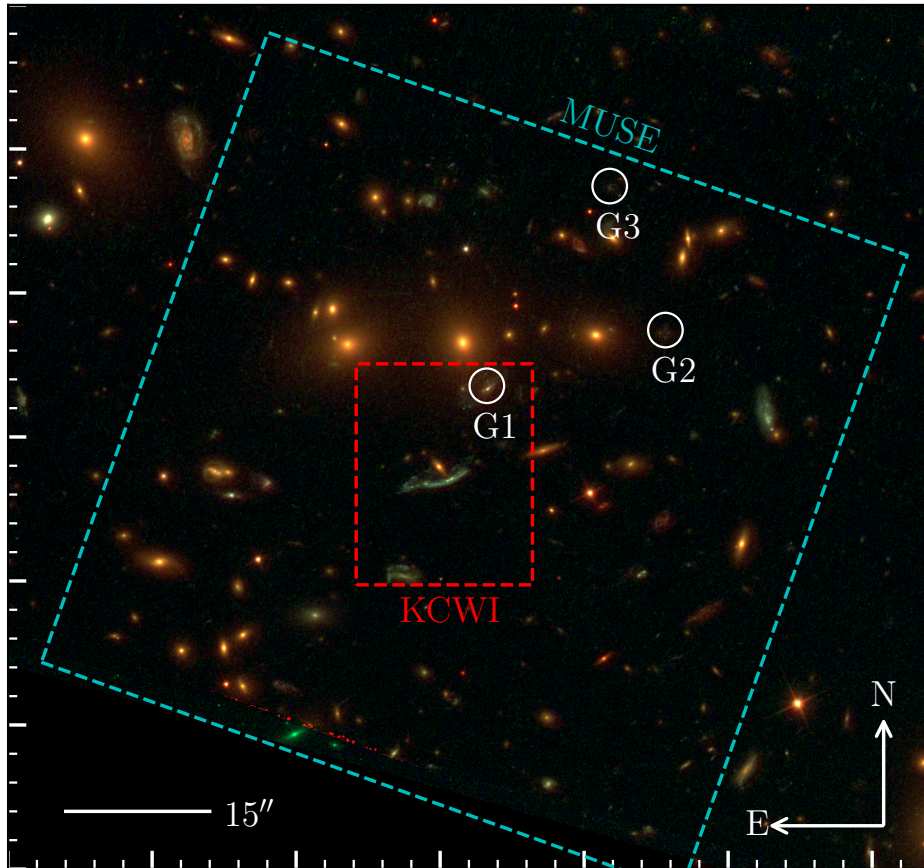


**Figure 1.** *Hubble Space Telescope* (HST) RGB image of the field of view (FoV) of the system SGASJ1527. We use WFC3 filters IR-F110W, UVIS-F606W, and UVIS-F475W for the red, green, and blue channels, respectively. The cyan and red dashed polygons mark the boundaries of the MUSE ( $60'' \times 60''$ ) and KCWI ( $16.5'' \times 20.4''$ ) IFU spatial coverages, respectively. The three white circles mark three galaxies, which are members of the same group at  $z \approx 0.785$ . The three galaxies are shown in the right column from top to bottom, respectively, from the HST WFC3-IR-F110W, where they show the highest magnitudes. The galaxy G1 is the main target that shows a signature of an outflow. The arc in the middle of the KCWI FoV is of a galaxy at  $z \approx 2.76$ .

IFU spectroscopy observation from the Keck Cosmic Web Imager KCWI (KCWI; [Morrissey et al. 2018](#)) was obtained for this field, (Program IDs: N080 and K338) in 2018 and 2019, respectively. The total exposure time is 3.56 hours from both observations (N080: 1.56 hours, K338: 2 hours). We refer the reader to [Bordoloi et al. \(2022\)](#) for the full details of observations and data reduction. Here, we give a summary of the observational details. Observations were obtained with the BL grating and the medium IFU slicer, giving a total field of view of  $16.5'' \times 20.4''$ , and a spectral resolution  $R = 1800$ . These observations have a wavelength coverage of 350–550 nm. The average seeing during the observing period was  $\approx 0.8''$ . Data were reduced using the KCWI data reduction pipeline `KCWI_DRP`<sup>1</sup> ([Neill et al. 2023](#)) and

individual frames were astrometry corrected, trimmed and co-added after resampling the individual spaxels to a square spaxel grid using the `kcwitoools` package ([O’Meara et al. 2022](#)). Frames were resampled using `Montage`<sup>2</sup> ([Jacob et al. 2010a,b](#)).

Publicly available VLT/Multi Unit Spectroscopic Explorer (MUSE; [Bacon et al. 2010](#)) observations are obtained for this field from the ESO archive (Program ID: 0103.A-0485(B), PI: S. Lopez) ([Lopez et al. 2024](#); [Berg et al. 2024](#)). The MUSE observations were taken in 2019 with a total exposure time of  $\approx 4$  hours. The seeing during observations was in the range of  $0.82''$ – $0.87''$ . MUSE has a wavelength coverage of 459.96 – 935.08 nm (extended range) and a spectral resolution of  $R = \frac{\lambda}{\Delta\lambda} \approx 2989$  at the central wavelength for this

<sup>1</sup> <https://kcwi-drp.readthedocs.io/>

<sup>2</sup> <http://montage.ipac.caltech.edu/>

observation. The mode of observation was Wide Field Mode (WFM) with Adaptive Optics (AO) covering a field of view of  $60'' \times 60''$ , with a spatial pixel size of  $0.2'' \times 0.2''$ . The datacube is reduced using the MUSE public data reduction pipeline (Weilbacher et al. 2016, 2020). In the resulting datacube, the observed wavelength values are measured in air. Therefore, we perform air-to-vacuum correction for the wavelength values. Upon initial inspection of the datacube, we notice the presence of some strong skylines in the spectra. To remove these skylines, we use the Zurich Atmospheric Purge (ZAP) algorithm to clean the datacube from their contribution (Soto et al. 2016). We create a source mask using `photutils`<sup>3</sup> (Bradley et al. 2023), to identify all bright sources in the field. This mask was fed into ZAP before performing the sky subtraction step. This creates the final sky-subtracted MUSE datacube used in this analysis.

Both the KCWI and MUSE datacubes are astrometry corrected to ensure that all observations have accurate and consistent spatial information. We perform this astrometric correction with a custom script that is described as follows. The ground-based observations are astrometry corrected to match the WCS solution of the HST observations (see §2.2 for HST observations description). First white light images are created for both KCWI and MUSE datacubes. Then, using `photutils`, bright sources are detected in both the white light images and in the HST image. At least three common bright sources are identified in each image, and the astrometric difference between them with respect to the HST image is calculated. We find an astrometric offset in the KCWI cube coordinates with respect to the space-based HST observations to be  $\Delta\alpha = 0.38''$  in right ascension ( $\alpha$ ), and  $\Delta\delta = 1.34''$  in declination ( $\delta$ ), respectively. Similarly, we find an astrometric offset of  $\Delta\alpha = 0.82''$  and  $\Delta\delta = 2.14''$  in the MUSE datacube. These offsets are applied as astrometric corrections to each IFU datacube separately.

Figure 2 shows the astrometry-matched observations from KCWI (left panel), MUSE (middle panel) as white-light images, and from HST as an RGB image (right panel). The galaxy of interest in this work (G1) at  $z = 0.785273$  (cyan square) and the lensed arc of the background galaxy at  $z \approx 2.76$  are marked in these panels of Figure 2. We sum the flux along the wavelength axis for KCWI and MUSE cubes to obtain 2D surface brightness white-light images (see Shaban et al. 2022 for details).

## 2.2. Photometric Observations

This field has been imaged with the Hubble Space Telescope (HST)- Wide Field Camera 3 (WFC3) (Proposal ID: 13003). These observations are with IR-F160W, IR-F110W, UVIS-F606W and UVIS-F475W, with exposure times 1211s, 1111s, 2400s, and 2400s, respectively. We use the filters F110W, F606W, and F475W to construct an RGB image of the FoV and match the astrometry of the ground-based IFU observations. The HST-WFC3 RGB image is shown in Figure 1 and in the right panel of Figure 2.

The same field has photometry from *Sloan Digital Sky Survey* (SDSS: Fukugita et al. 1996; Doi et al. 2010) from the filters  $u$ ,  $g$ ,  $r$ ,  $i$ , and  $z$ . Each of the observations from these filters has a total exposure of 53.9 seconds. In addition, there are available photometric observations from the *Panoramic Survey Telescope and Rapid Response System* (PanSTARRS: Tonry et al. 2012; Chambers et al. 2016) with filters  $g$ ,  $r$ ,  $i$ ,  $z$  and  $y$ . The exposure times of these observations are 853s, 668s, 1530s, 510s, and 780s, respectively.

We use `photutils` to estimate the flux in the aperture of G1 in all the filters from HST, SDSS, and PanSTARRS. We also estimate the flux in an empty background region in the field of view without any light sources to calculate the background flux. Then, we subtract this background flux from G1’s aperture flux to calculate the AB magnitudes using this background-subtracted flux and the zero point of each filter. We estimate the error on the AB magnitudes of G1 using the standard deviation of the flux in the background aperture times the square root of the area of the G1’s aperture.

We use these photometric AB magnitudes to perform SED fitting to characterize the stellar properties of G1 (see §3.3).

## 3. METHODS

In this section, we describe the methods used to extract 1D spectra from the IFU datacubes, to estimate galaxy properties, model the SED, create emission line maps, estimate the outflow properties, and ray-trace measurements from image plane to the source-plane of G1.

### 3.1. Extracting the Spectra

<sup>3</sup> <https://photutils.readthedocs.io/en/stable/>

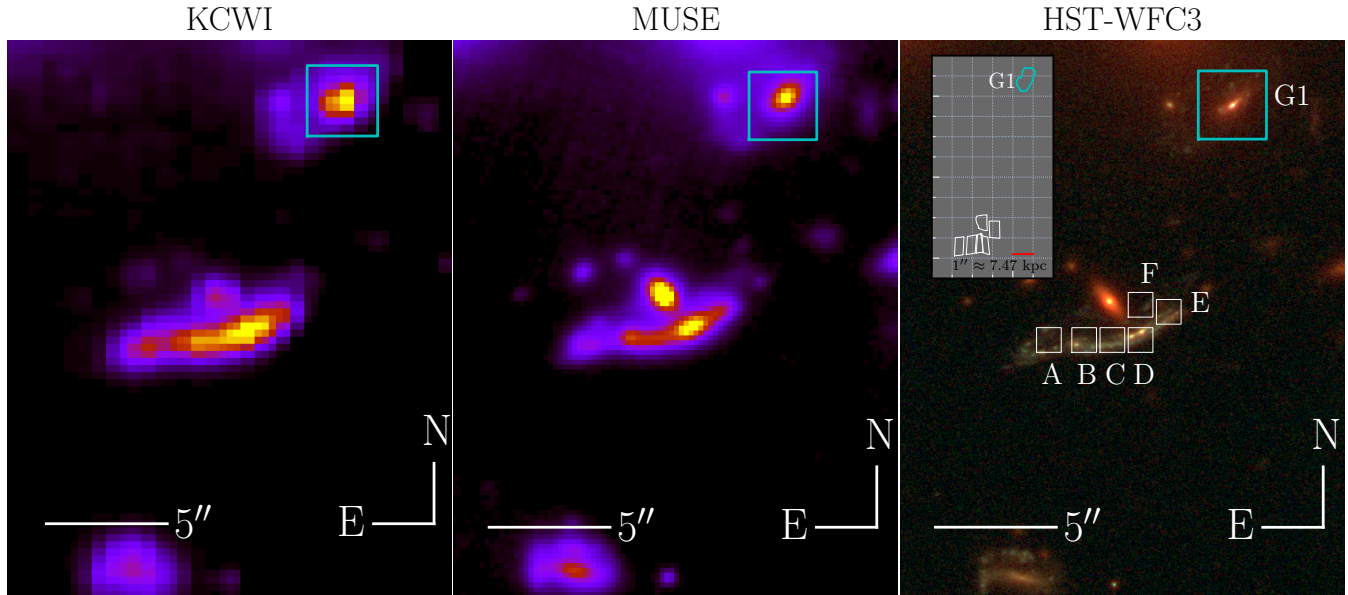


**Figure 2.** Field of view centered on the gravitationally lensed arc SGASJ1527 at  $z = 2.76$ . The galaxy of interest G1 at  $z = 0.785273$  is marked with a cyan square. White-light images from KCWI observations (left panel) and from MUSE observations (middle panel) are shown. The six apertures (each is  $1'' \times 1''$ ) across the arc, where individual 1D spectra are extracted, are marked on the HST/WFC3 image (right panel). The distances from the center of the galaxy to the arc are in the range of 54–66 kpc (see §3.2). The small light source to the east of G1 is an interloping foreground galaxy at  $z \approx 0.431$ . The inset in the right panel is the ray-traced locations of G1 and the apertures along the arc in the plane of G1. The grid squares have a size of  $1'' \times 1''$ , where  $1'' \approx 7.47$  kpc at the redshift of G1. The angular and physical separations between the apertures along the arc and G1 are presented in Table 1.

We use `kcwitoools`<sup>4</sup>(O’Meara et al. 2022) and `musetools`<sup>5</sup> to read the datacubes and optimally extract 1D spectra from both KCWI and MUSE observations, respectively. Along each aperture, we optimally extract 1D white light-weighted spectrum (see Bordoloi et al. 2022; Shaban et al. 2023 for details). Along the arc, apertures are chosen following Bordoloi et al. (2022) and are  $\approx 1'' \times 1''$  in size. The aperture for the galaxy G1 is  $\approx 3'' \times 3''$  and shown as a cyan square in Figure 2. This aperture captures the stellar light of G1, as shown in the HST image. The separation distances between G1 and the apertures in the plane of G1 are summarized in Table 1.

The 1D extracted spectra for galaxy G1 from KCWI and MUSE are shown in Figure 3. The bluer part of the spectrum extracted from KCWI (black line), shows several resonant absorption features: Mg II 2796, 2803 Å, and Fe II 2344, 2374, 2382, 2586, 2600 Å. Further several fine-structure emission lines: Fe II\* 2365, 2396, 2612, 2626, and 2632 Å are detected.

In the MUSE spectrum (blue line), a series of prominent emission lines, e.g., [O II] 3727, 3729 Å, [O III] 4960,

5008 Å, and the Hydrogen Balmer Series lines  $H\beta$ ,  $H\gamma$ ,  $H\delta$ , and  $H\epsilon$  are detected. Additionally, resonant absorption lines: Mg II 2796, 2803 Å, and Fe II 2586 Å, 2600 Å lines are detected. Along with these lines, three weak Fe II\* fine-structure emission lines: Fe II\* 2612, 2626, and 2632 Å are detected. We summarize the important lines used in this analysis in Table 2.

The combination of both KCWI and MUSE spectrographs allow simultaneous investigation of the rest frame spectra of galaxy G1 from near-UV to optical ( $2000 \leq \lambda/\text{Å} \leq 5200$ ). The KCWI and MUSE spectrographs overlap in the wavelength range between  $\lambda_{rest} = 2580 - 2640$  Å ( $\lambda_{observed} = 4606 - 5713$  Å). In this wavelength range, Mg II 2796, 2803 Å, Fe II 2586, 2600 Å, and Fe II\* 2612, 2626, 2632 Å are detected in both spectrographs. We leverage this information and simultaneously fit these lines while accounting for different line spread functions (LSF) (see §3.6). This allows us to increase the signal-to-noise of the final fits while simultaneously accounting for different resolutions of the two instruments.

In addition to the galaxy, we extract 6 spectra across the lensed arc in Figure 2 from both IFU observations. These sightlines probe the CGM of galaxy G1. Each one of these spectra is extracted from square aperture with size  $1'' \times 1''$ , shown as white squares in the right panel

<sup>4</sup> <https://github.com/pypeit/kcwitoools>

<sup>5</sup> <https://github.com/rongmon/musetools>

**Table 1.** Coordinates and properties of the galaxy G1 and apertures across the SGAS J1527 arc.

Aperture	$\alpha^a$	$\delta^a$	$\Delta\theta_{G1,i}^b$	$D_{G1,i}^c$	$W_{r,MgII2796}^d$
	J2000	J2000	["]	[kpc]	[Å]
(1)	(2)	(3)	(4)	(5)	(6)
G1	15:27:44.851	+06:52:29.076	–	–	$1.97^{+0.06}_{-0.06}$
A	15:27:45.360	+06:52:19.359	8.8	$65.7^{+1.0}_{-1.1}$	$0.33^{+0.08}_{-0.07}$
B	15:27:45.262	+06:52:19.359	8.5	$63.5^{+1.2}_{-1.1}$	$0.64^{+0.06}_{-0.06}$
C	15:27:45.184	+06:52:19.359	8.3	$62.1^{+1.5}_{-1.1}$	$0.48^{+0.06}_{-0.05}$
D	15:27:45.105	+06:52:19.359	8.3	$62.0^{+1.6}_{-1.3}$	$0.36^{+0.04}_{-0.04}$
E	15:27:45.027	+06:52:20.524	7.4	$55.0^{+1.4}_{-1.1}$	$0.29^{+0.06}_{-0.06}$
F	15:27:45.105	+06:52:20.816	7.2	$53.9^{+1.1}_{-1.0}$	$0.30^{+0.08}_{-0.07}$

<sup>a</sup>All coordinates are in image plane.

<sup>b</sup>Angular separation from G1 is measured in the plane of G1.

<sup>c</sup>Physical separation from G1 is measured in the plane of G1.

<sup>d</sup>Rest-frame equivalent width of Mg II 2796 absorption

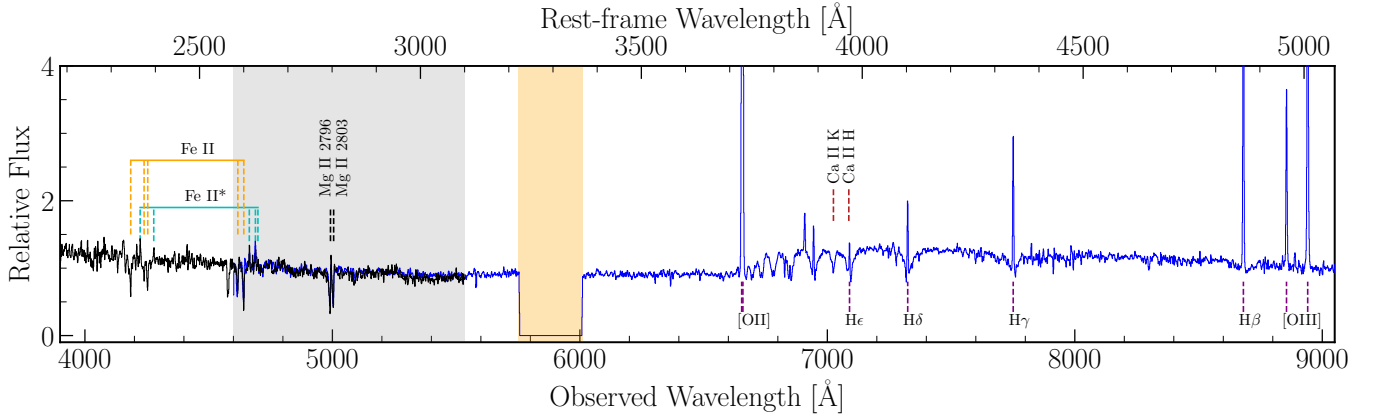


**Figure 3.** Optimally extracted 1D spectrum of galaxy G1 at  $z \approx 0.78$  (cyan square, Figure 2). 1D spectra from KCWI and MUSE datacubes are marked as black and blue solid lines, respectively. The bottom and top x-axes represent the observed and rest-frame wavelengths, respectively. The overlapping wavelength range between the two instruments is marked as the gray vertical band. The wide gap (faint orange band) around  $\lambda_{observed} \approx 5800 - 6000$  Å is the wavelength band of the Sodium D-line laser used in the MUSE Adaptive Optics (AO) mode. The spectra are smoothed with a 3 pixel moving average kernel for presentation. Prominent emission/absorption lines are marked with vertical dashed lines (see Table 2).

of Figure 2. We detect Mg II 2796, 2803 Å absorption at the redshift of galaxy G1 along these sightlines. The coordinates of G1 and the six apertures across the arc are summarized in Table 1. Table 1 also includes the angular separations between the apertures along the arc and the center of G1, measured in G1’s plane.

Before modeling the transitions of interest, each spectrum is continuum-normalized. This is done locally by fitting a 3rd order polynomial to a 75 Å region around each transition. The flux around this region is di-

vided by the local continuum to obtain the continuum-normalized flux around these transitions. These continuum normalized spectra are used to perform absorption/emission line strength measurements.

### 3.2. Ray-tracing and Lens Model

In order to calculate the distances from G1 to the sightlines along the arc, we need to account for the effect of gravitational lensing due to the foreground galaxy cluster. This galaxy cluster is at redshift

**Table 2.** Prominent absorption and emission lines in the spectrum of the galaxy G1.

Transition <sup>a</sup>	$\lambda^b$	Feature	$f_0^c$	KCWI	MUSE
Fe II	2344.212	Resonant abs	0.1142	Yes	No
	2374.460	Resonant abs	0.0313	Yes	No
	2382.764	Resonant abs	0.320	Yes	No
	2586.650	Resonant abs	0.069125	Yes	Yes
	2600.173	Resonant abs	0.2394	Yes	Yes
Fe II*	2365.552	Fine-structure ems	–	Yes	No
	2396.355	Fine-structure ems	–	Yes	No
	2612.654	Fine-structure ems	–	Yes	Yes
	2626.451	Fine-structure ems	–	Yes	Yes
	2632.108	Fine-structure ems	–	Yes	Yes
Mg II	2796.351	Resonant abs/ems	0.6155	Yes	Yes
	2803.528	Resonant abs/ems	0.3058	Yes	Yes
[O II]	3727.092	Nebular Emission	–	No	Yes
	3729.874	Nebular Emission	–	No	Yes
H $\epsilon$	3971.198	Emission	–	No	Yes
H $\delta$	4102.892	Emission	–	No	Yes
H $\gamma$	4341.692	Emission	–	No	Yes
H $\beta$	4862.708	Emission	–	No	Yes
[O III]	4960.295	Emission	–	No	Yes
[O III]	5008.239	Emission	–	No	Yes

<sup>a</sup>Atomic data from Morton (2003) and Leitherer et al. (2011)

<sup>b</sup>Vacuum wavelength in angstroms Å.

<sup>c</sup>Oscillator Strengths

$z = 0.392 \pm 0.005$  (Bayliss et al. 2011). We follow the ray-tracing procedure described in Bordoloi et al. (2022) and Shaban et al. (2023) to compute the physical separations between the center of G1 and the centers of the six sightlines across the arc in the plane of G1 at  $z = 0.785$  using the lens model from Sharon et al. (2020). We obtain the physical separations by multiplying the delensed angular separation, from the ray-tracing step, by the angular diameter distance  $D_A$  of G1 (Hogg 1999). The full details of the lens model are described in Bordoloi et al. (2022) and Sharon et al. (2020).

### 3.3. Estimating the Galaxy Properties

#### 3.3.1. Redshift and Star Formation Rate (SFR)

To estimate the redshift ( $z$ ) of galaxy G1, we fit the [O II]  $\lambda\lambda 3727, 3729$  doublet using a double Gaussian model and measure the systemic redshift to be  $z = 0.785273 \pm 0.000001$ . The double Gaussian model allows redshift to vary while keeping line ratios between the [O II] doublet constant. The model was fit using the affine-invariant

ensemble sampler `emcee` (Foreman-Mackey et al. 2013). Similarly, we measure the redshifts of the galaxies G2 and G3 to be  $0.78494 \pm 0.00001$  and  $0.78542 \pm 0.00001$  using their MUSE spectra.

Emission lines like [O II] and H $\beta$  are excellent tracers for measuring star-formation rates (SFR) in galaxies (Kennicutt 1998). Before we measure the fluxes of these lines to calculate the SFR for G1, we need to account for the interstellar dust extinction on G1’s spectrum by de-reddening the spectrum. This requires the calculation of the color excess  $E(B - V)$ . We calculate  $E(B - V)$  using the observed fluxes ratio of the H $\gamma$  and H $\beta$  emission lines and compare it to the intrinsic lines ratio  $(H\gamma/H\beta)_{int} = 0.469$  in case B recombination, which is the standard case in HII regions (Osterbrock & Ferland 2006). By measuring the fluxes of the H $\gamma$  and H $\beta$  using a model consisting of a Gaussian and 1D polynomial, we estimate the observed ratio to be  $(H\gamma/H\beta)_{obs} = 0.346$ . By using attenuation law from Calzetti et al. (2000), which is suitable to describe the effects of dust attenuation in star-forming galaxies, particularly at ultravi-

olet (UV) and optical wavelengths, we obtain a color excess  $E(B - V) = 0.628$  for G1. For de-reddening the spectrum, we use the `dust_extinction` module from `astropy` (Astropy Collaboration et al. 2013, 2018, 2022) with a dust extinction law from Fitzpatrick (1999) with total-to-selective extinction ratio of  $R_V = 3.1$  for the Milky Way (Cardelli et al. 1989). From the de-reddened spectrum of G1, we measure the total flux of the  $H\beta$  line by fitting a model consisting of 1D polynomial for the continuum and a Gaussian for the emission line. From the total flux and the angular diameter distance to the galaxy, we obtain the  $H\beta$  luminosity  $L_{H\beta}$  that is related to  $H\alpha$  luminosity  $L_{H\alpha} = 2.86L_{H\beta}$  (Osterbrock & Ferland 2006). We use the scaling relation between SFR and  $L_{H\alpha}$  from Kennicutt (1998) to obtain an SFR =  $30.8 \pm 0.5 M_\odot \text{ yr}^{-1}$  for G1.

### 3.3.2. Spectral Energy Distribution (SED) Fitting

In order to obtain the stellar properties of the galaxy, we perform SED fitting using the photometric measurements from HST, PanSTARRS, and SDSS. We use `photutils` to perform aperture photometry to obtain the magnitudes of G1 and the corresponding photometric uncertainties across the different photometric bands (see §2.2).

We perform the SED fitting using `prospector`<sup>6</sup> (Johnson et al. 2021). `prospector` uses the flexible stellar population synthesis model from Conroy et al. (2009); Conroy & Gunn (2010) and its python implementation `python-FSPS` (Johnson et al. 2023). We assume a simple parametric decaying star-formation history (SFH):  $SFH \propto e^{-t_l/\tau}$ , where  $t_l$  is the look-back time, and  $\tau$  is the characteristic timescale for SFH, which is one of the free parameters of our SED model. The other free parameters for this model are the stellar mass  $M_*$ , the dust extinction  $A_V$ , the age  $t_{age}$  of the galaxy at the measured redshift, and the stellar metallicity  $Z_*$ . In addition, we use the nebular emission template that has the gas metallicity  $Z_{gas}$ , and gas ionization parameter  $U$  as free parameters to reproduce the emission lines of G1. To sample the posterior distribution of the model parameters, we use the nested-sampling using `dynesty`<sup>7</sup> option in `prospector` (Speagle 2020; Koposov et al. 2023). We estimate the stellar mass of G1 to be  $\log(M_*/M_\odot) = 10.84^{+0.13}_{-0.10}$ . From the stellar mass, we estimate the dark matter halo mass of G1 to be  $\log(M_{halo}/M_\odot) = 12.90^{+0.64}_{-0.34}$  (Behroozi et al. 2019).

### 3.4. Emission Maps

To obtain the 2D surface brightness images of the emission lines in G1 spectrum, we follow the procedure described in Shaban et al. (2022). We select two wavelength windows of equal size: the first window to incorporate the emission line of interest along with the underlying stellar continuum, and the second window to include only the stellar continuum of the galaxy (Figure 4, top panels). Flux from each spatial pixel (spaxel)  $(i, j)$  in these wavelength windows are summed to obtain the surface brightness  $SB_{(i,j)}$  images as follows:

$$SB_{(i,j)} = \frac{\delta\lambda}{\Delta xy} \sum_{l=\lambda_{min}}^{l=\lambda_{max}} f_{(l,i,j)}, \quad (1)$$

where  $f_{(l,i,j)}$  is the flux density at the voxel  $(l, i, j)$  in units of  $\text{erg s}^{-1} \text{ cm}^{-2} \text{ \AA}$ ,  $\delta\lambda$  is the size of the pixel along the wavelength axis ( $\delta\lambda_{MUSE} = 1.25 \text{ \AA}$ ,  $\delta\lambda_{KCWI} = 1 \text{ \AA}$ ), and  $\Delta xy$  is the angular area of the spaxel ( $\Delta xy_{MUSE} = (0.2'')^2$ ,  $\Delta xy_{KCWI} = (0.29'')^2$ ). Finally, the image containing stellar continuum is subtracted from the emission+continuum image to obtain the continuum-subtracted emission maps.

### 3.5. Models of galactic outflow and CGM absorption

We first describe the models used to quantify the ‘down-the-barrel’ blueshifted absorption in the galaxy G1 seen in Mg II and Fe II absorption lines. We refer the readers to Shaban et al. (2023) for more details of the outflow models. In brief, we model the continuum-normalized flux as:

$$F(\lambda) = 1 - C_f(\lambda) + C_f(\lambda)e^{-\tau(\lambda)}, \quad (2)$$

where  $C_f(\lambda)$  and  $\tau(\lambda)$  are the covering fraction and optical depth as functions of wavelength, respectively (Rupke et al. 2005; Sato et al. 2009; Rubin et al. 2014). The optical depth  $\tau(\lambda)$  can be expressed as a function of rest-frame wavelength of each transition ( $\lambda_0$ ) and the optical depth ( $\tau_0$ ) at the center of the absorption line as:

$$\tau(\lambda) = \tau_0 e^{(\lambda - \lambda_0)^2 / (\lambda_0 b_D / c)^2}. \quad (3)$$

Here,  $b_D$  is the Doppler velocity width, and  $c$  is the speed of light in vacuum. Also  $\tau_0$  is defined in terms of  $\lambda_0$ ,  $b_D$ , the column density  $N$ , and the oscillator strength  $f_0$  of the transition as (Draine 2011):

$$N[\text{cm}^{-2}] = \frac{\tau_0 b_D [\text{km s}^{-1}]}{1.497 \times 10^{-15} \lambda_0 [\text{\AA}] f_0}. \quad (4)$$

We link all the absorption lines of the same ionic transition using the line ratios, which are allowed to vary as free parameters of the model. It is worth noting that the Mg II absorption doublet is saturated in G1 spectrum,

<sup>6</sup> <https://prospect.readthedocs.io/en/latest/>

<sup>7</sup> <https://github.com/joshspeagle/dynesty>

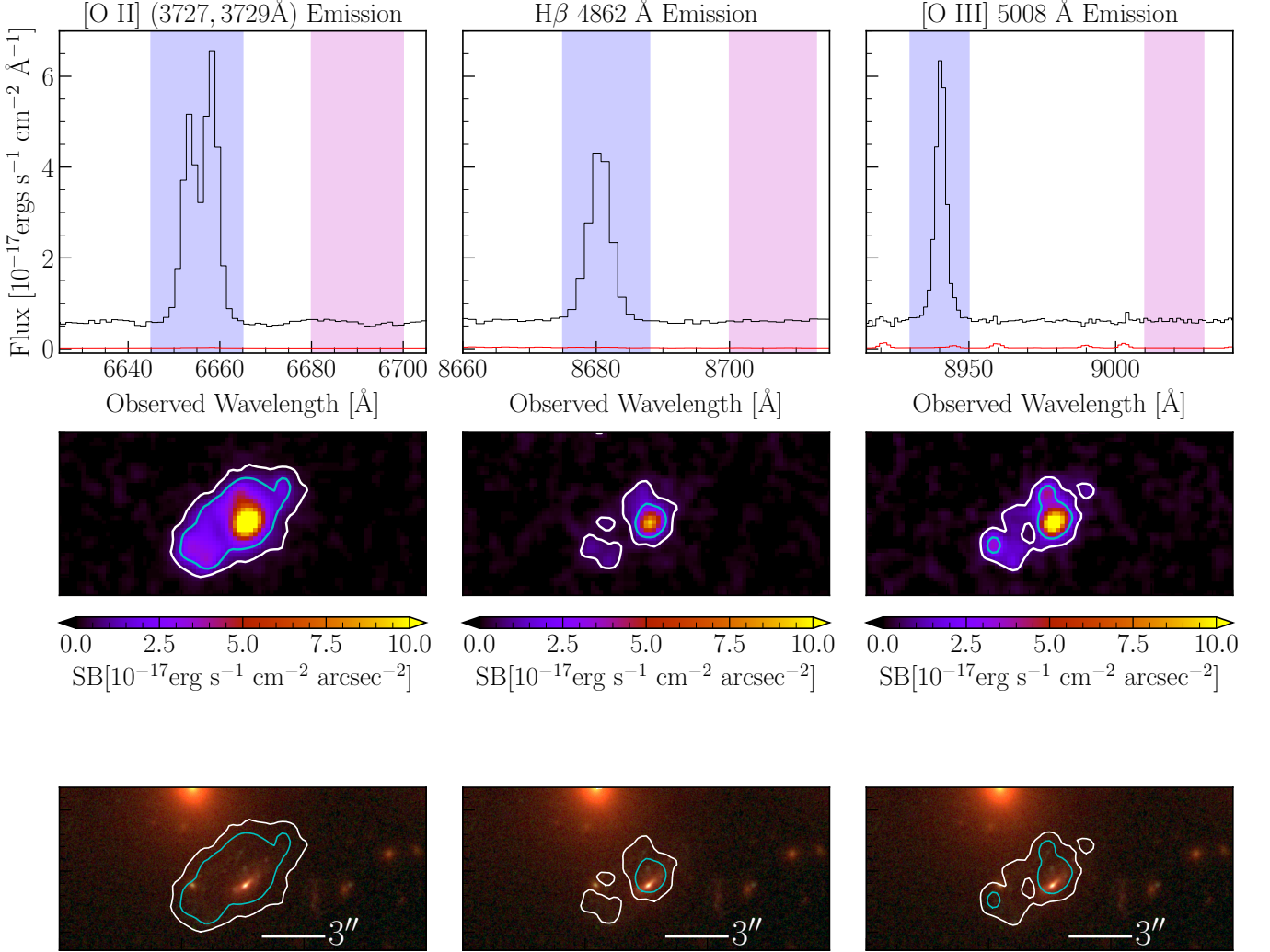


**Figure 4.** *Top row:* Prominent emission lines in the galaxy: [O II] 3727, 3729 Å (*Left column*),  $H\beta$  (*Middle column*), and [O III] 5008 Å (*Right column*) from MUSE, respectively. The solid black and red lines are the flux and the associated uncertainty, respectively. The faint blue and faint magenta windows represent the wavelength windows used to compute the surface brightness maps of emission+stellar continuum and stellar continuum only, respectively. *Middle row:* The surface brightness maps of the continuum-subtracted emission (blue - magenta from top row) around galaxy G1. The white and cyan contours are the  $3\sigma$  and  $10\sigma$  background surface brightness levels. *Bottom row:* HST/RGB image of the galaxy, with surface brightness contours from the middle row overlaid. The white horizontal  $3''$  bars in bottom panels corresponds to  $\approx 10$  kpc in the plane of G1.

therefore the total column density of the outflowing gas is strictly a lower limit. For the emission lines, We model each emission line as a Gaussian:

$$F_{ems}(\lambda) = 1 + G(\lambda; A, v_0, b_D), \quad (5)$$

where the parameters  $A$ ,  $v_0$ ,  $b_D$  are the amplitude, the central velocity and the Doppler velocity width of the emission line, respectively. Similar to the absorption lines, we link the amplitudes of the different emission lines of the same species together using the line ratios, which are free parameters of the model (Shaban et al. 2023).

For the absorption and emission lines in the galaxy G1, the final model has two components: outflowing ( $F_{out}(\lambda)$ ) and emission ( $F_{ems}(\lambda)$ , equation 5). We enforce a prior to exclusively consider only blueshifted velocities as outflowing component (see Shaban et al. 2023). The final model is convolved with the line spread function (LSF) of the instrument. Visual inspection of the ‘down-the-barrel’ galaxy G1 spectrum shows that Mg II and Fe II lines have two distinct kinematic components. We account for it by incorporating a second outflowing component to model the high velocity part of these lines.

The six spectra towards the lensed arc at  $z \approx 2.76$  detect Mg II absorption associated with galaxy G1 at  $z \approx 0.8$ . These are modeled with a double Gaussian where the line ratios between the two Gaussian components are between 1-2, and the line separation between them is set at  $786 \text{ km s}^{-1}$ .

### 3.6. Fitting the Models

The models described above are fitted to the 1D spectra around the transitions of interest using the affine invariant Markov chain Monte Carlo sampler `emcee` (Foreman-Mackey et al. 2013). This sampler uses Bayesian inference to sample the posterior probability density function (PPDF) of the model parameters. Uniform priors on each model parameter are assumed as described in the previous section. We use a total of 50 walkers, with a total number of 50000 steps. The first 5000 steps are used for the burn-in time.

Since we have observations from two instruments (MUSE, KCWI), we simultaneously fit the spectra with the same underlying model when both are available. KCWI has a bluer wavelength coverage, therefore it covers Fe II transitions down to  $2344 \text{ \AA}$ . MUSE spectra can detect Fe II transitions down to  $2586 \text{ \AA}$ . A joint likelihood function is written to account for data from both the instruments. In this case, the log-likelihood  $\log(\mathcal{L})$  can be written as:

$$\log(\mathcal{L}(\vec{\theta})) \propto -\frac{1}{2} \sum_{j=1}^{N_K} \left( \frac{F(\lambda_{K,j}; \vec{\theta})_{K,j} - y_{K,j}}{\sigma_{K,j}} \right)^2 - \frac{1}{2} \sum_{j=N_K+1}^{N_K+N_M} \left( \frac{F(\lambda_{M,j}; \vec{\theta})_{M,j} - y_{M,j}}{\sigma_{M,j}} \right)^2, \quad (6)$$

where  $F(\lambda; \vec{\theta})_K$  and  $F(\lambda; \vec{\theta})_M$  are the same physical model for an ionic transition convolved with the LSFs for KCWI and MUSE, respectively.  $\vec{\theta}$  are the model parameters,  $y_{K,j}$  and  $\sigma_{K,j}$  are the  $j^{\text{th}}$  data points of KCWI flux and flux uncertainty, respectively,  $y_{M,j}$  and  $\sigma_{M,j}$  are the  $j^{\text{th}}$  data points of MUSE flux and flux uncertainty, respectively.  $N_K$  and  $N_M$  represent the total number of data points of the normalized spectrum of the same transition from KCWI and MUSE, respectively.

From the `emcee` PPDFs realizations of the model parameters of this joint fit, we calculate the rest-frame equivalent width  $W_r$ , and the weighted outflow velocity  $V_{out}$  for each realization as described in Shaban et al. (2023). The final best fit results are shown in Figure 7 and Figure 8.

## 4. RESULTS AND DISCUSSION

### 4.1. Emission maps

Several strong emission lines are detected in the spectrum of galaxy G1 (Figure 3). In this section, we quantify the spatial extent of these strong emission features. Continuum-subtracted surface brightness maps for [O II] $\lambda\lambda$  3727, 3729,  $H\beta$ , and [O III] $\lambda$ 5008 lines are produced as described in §3.4. The wavelength windows used to select the emission+stellar continuum regions and the continuum only regions are shown in the top row of Figure 4. The rest-frame sizes of these wavelength windows are  $11.2 \text{ \AA}$ ,  $7.3 \text{ \AA}$ , and  $11.2 \text{ \AA}$  ( $20 \text{ \AA}$ ,  $13 \text{ \AA}$ , and  $20 \text{ \AA}$  in the observed frame) for the [O II],  $H\beta$ , and [O III] emission lines, respectively.

Figure 4, middle row, shows the continuum-subtracted emission maps for these lines. The white and cyan contours represent the  $3\sigma$  and  $10\sigma$  surface brightness noise levels associated with the maps. The  $1\sigma$  values are computed by selecting an empty region in this FoV with angular size of  $4'' \times 4''$ . The  $1\sigma$  surface brightness noise level is  $1.39 \times 10^{-18}$ ,  $1.83 \times 10^{-18}$ , and  $2.59 \times 10^{-18} \text{ erg s}^{-1} \text{ cm}^{-2} \text{ arcsec}^{-2}$  for [O II],  $H\beta$ , and [O III] emission maps, respectively.

Figure 4, bottom row, shows the HST/RGB images of galaxy G1 with the contours from the middle panel overlaid. The [O II] emission halo at  $3\sigma$  level has the maximum physical spatial extent of  $\approx 33.4 \text{ kpc}$  in the plane of G1 at  $z \approx 0.8$ . The  $H\beta$  and [O III] emission maps are less spatially extended and show two distinct emission components. This might be because the [O II] emission lines are the strongest lines in this spectrum.

The emission maps can be used to measure the mean flux weighted velocity  $\langle v \rangle$  (first moment) and the velocity dispersion  $\sigma_v$  (second moment) of each spaxel. At each spaxel, a local continuum (first order 1D polynomial) and a Gaussian is fitted around each line of interest. The fitted Gaussian profile is used to compute the  $\langle v \rangle$  and  $\sigma_v$  for each emission line. Figure 5 shows  $\langle v \rangle$  for all spaxels that are greater than  $3\sigma$  detection level. For [O II] doublet, the kinematics of the [O II] 3727 line is presented. A clear velocity gradient is seen across the major axis of the galaxy for all three emission lines. We note that the gas distribution is asymmetric, with emission detected along the minor axis of the galaxy. Additionally, the velocity profile shows a skewed distribution, which is inconsistent with a pure rotating disk. Evidence of rotation is also detected in the CGM kinematics of Mg II absorbers using QSO and background lensed arc absorption line spectroscopy (Ho et al. 2017; Martin et al. 2019; Tejos et al. 2021). However, in this case, it is possible that we are detecting a combination of co-rotating halo gas and recycled material from outflows, creating the observed complex kinematic profile. The

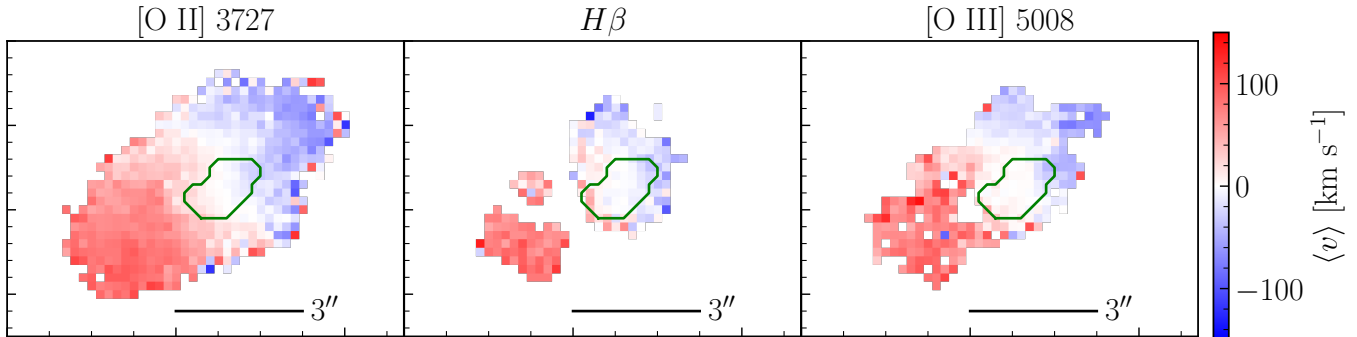


**Figure 5.** The mean weighted velocity per pixel (first moment) as measured from the emission lines [O II] 3727 (*left panel*),  $H\beta$  (*middle panel*), and [O III] 5008 (*right panel*) for the galaxy G1. The green contour represents the stellar light size of G1 as measured from HST-WFC3 F606W. All the velocity maps show a gradient in velocity from redshifted velocities on the left side to blueshifted velocities on the right side of G1. This is the kinematic signature of a rotating disc. The pixels beyond the green contour are emission from the gaseous halo around G1. The 3'' black line marker corresponds to  $\approx 10$  kpc in the plane of G1.

velocity gradient spans a velocity range of  $170 \text{ km s}^{-1}$ . The velocity dispersion ( $\sigma_v$ ) is of the order of the resolution element of MUSE ( $\sim 60 - 100 \text{ km s}^{-1}$ ) and this work cannot disentangle any variation in  $\sigma_v$  in this system. This system is an interesting case with a large co-rotating gas-halo of a star-forming galaxy, which is also driving a strong galactic outflow (see §4.2)(e.g., Tejos et al. 2021).

The spatially extended emission line maps can be used to compute spatial variation of metallicity across the galaxy. The measured flux of the [O II]  $\lambda 3727$ ,  $H\beta$ , and [O III]  $\lambda 4960$ , 5008 lines are measured using the fitted Gaussians. We use the R23 line ratio:  $R23 = ([OII]_{3727} + [OIII]_{4960,5008})/H\beta$  (Pagel et al. 1979) and use the calibration between the Oxygen abundance  $12 + \log(O/H)$  and  $R23$  from Zaritsky et al. (1994):

$$12 + \log\left(\frac{O}{H}\right) = 9.265 - 0.33x - 0.202x^2 - 0.207x^3 - 0.333x^4, \quad (7)$$

where  $x = \log(R23)$ . As the available observations do not cover other emission lines like Si II, N II, and  $H\alpha$ , the R23 diagnostic and this calibration represent the current best way to estimate the metallicity from [O II], [O III], and  $H\beta$  lines (Kewley & Dopita 2002). Figure 6 presents the spatially resolved metallicity map of galaxy G1. The spaxels are color coded relative to solar metallicity. It is striking that the majority of the spaxels have inferred metallicities higher than solar. We use the light-weighted spectrum of G1 (Figure 3) to measure the average metallicity of galaxy G1 as  $12 + \log(O/H) = 8.99 \pm 0.04$ , which is  $1.03 \pm 0.01$  times the solar value. The high metallicity in a co-rotating gas-halo and a strong galactic outflow signature in the

‘down-the-barrel’ absorption suggests that this might be a unique case where the ‘galactic fountain’ is seen in action, enriched outflowing gas is falling back in, and co-rotating with the galaxy before losing angular momentum and falling farther into the galaxy (Stewart et al. 2013).

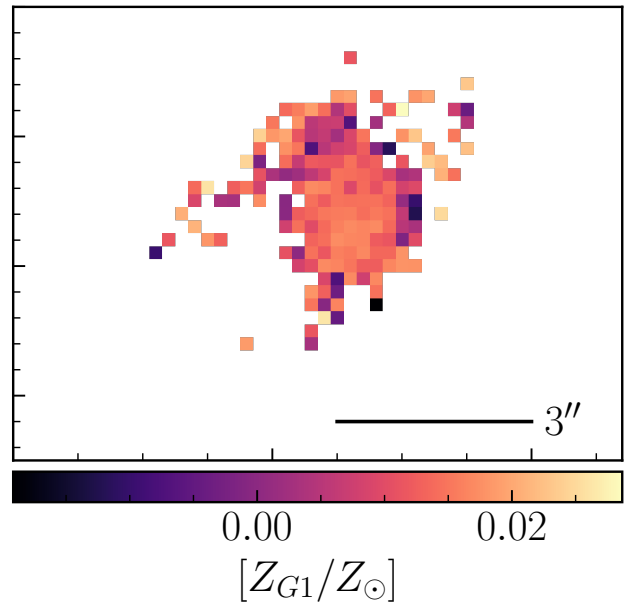


**Figure 6.** The ratio between the metallicity in each pixel in G1 and the photospheric solar metallicity (Asplund et al. 2021). Most of the pixels are higher than the solar value. The 3'' black line marker corresponds to  $\approx 10$  kpc in the plane of G1.

#### 4.2. Galactic Outflow properties

The galaxy G1 drives a strong galactic outflow seen as blueshifted Fe II and Mg II absorption lines. We mea-

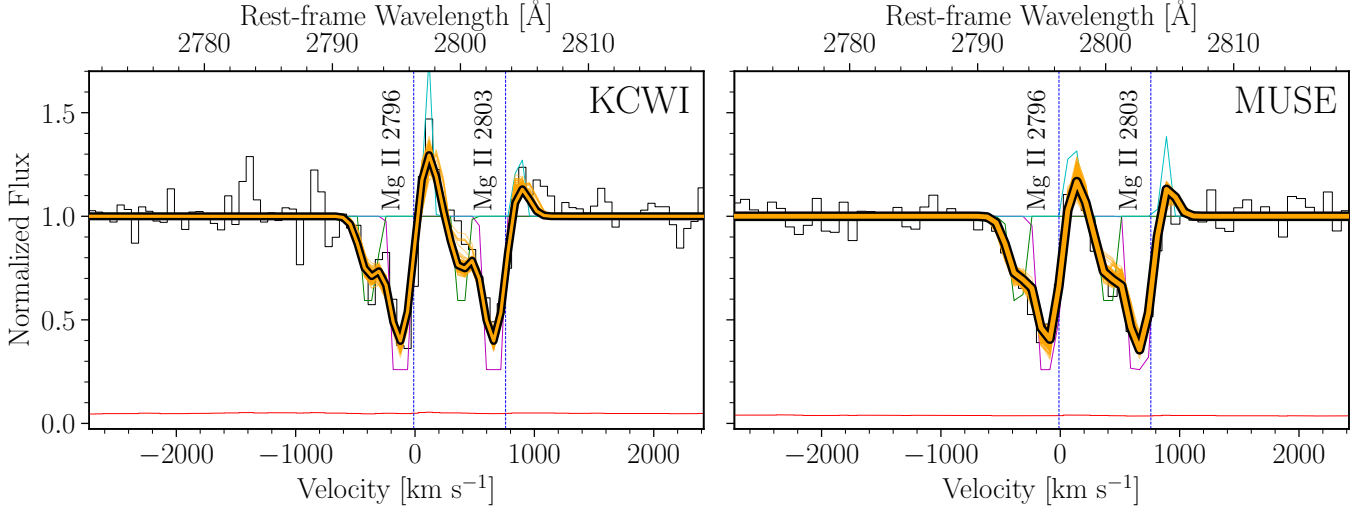


**Figure 7.** The Mg II 2796, 2803 Å doublet in galaxy G1 from KCWI (*Left Panel*) and MUSE (*Right Panel*), respectively. The solid black line and solid red line represent the normalized flux and normalized flux uncertainties. Velocities are centered on the Mg II 2796 transition at G1’s systemic redshift. The solid dark orange line is best fit outflow model convolved with the line spread function (LSF) for each instrument. The faint orange lines are 300 random realizations after sampling the posterior distribution. The purple and green lines for the first and second outflow components of the model. The cyan lines represent the emission component of the model.

sure these outflow properties and present them in this section.

We use the outflow model highlighted in §3.5 and fit an outflow model with two kinematic components to both the Mg II and Fe II transitions. We first report the outflow kinematics and column densities traced by Mg II absorption. Figure 7 shows the best fit outflow model (orange line) and 300 realizations of the outflow model (gray lines) created by randomly sampling the posterior distribution are presented. The spectra from KCWI and MUSE are simultaneously fitted, thereby incorporating maximum information into the fit.

We use the posterior distribution of the model parameters to measure an absorption weighted mean outflow velocity of  $V_{out} = -179^{+6}_{-5}$  km s<sup>-1</sup> from the two components model. The lower limit on the outflow column density traced by Mg II absorption is  $\log(N_{out}/\text{cm}^{-2}) \geq 15.83^{+0.23}_{-0.39}$ , where  $N_{out}$  is the sum of the column densities of the two individual outflowing components ( $N_{out} = N_{out,1} + N_{out,2}$ ). This corresponds to a rest frame equivalent width of the Mg II 2796 line as  $W_r = 1.97^{+0.06}_{-0.06}$  Å. The two outflow components have a gas covering fraction of  $C_{f,1} = 0.74^{+0.06}_{-0.03}$  for the first component and  $C_{f,2} = 0.41^{+0.03}_{-0.03}$  for the second component, respectively. The difference in  $C_f$  values, highlight that the outflowing gas at the highest velocities are less covered by the light from the background galaxy G1. This suggests that such high velocity gas is more patchy and is potentially probing gas much farther away than low velocity outflowing gas (e.g., Chisholm et al. 2018). However, since

Mg II 2796 line is the strongest absorption line reported in this work (and is not contaminated by emission filling), it is ideal to trace the highest velocity wing of the outflowing gas. We find that galaxy G1 has a maximum outflow velocity  $V_{95} = -415^{+10}_{-7}$  km s<sup>-1</sup>, which is the 95<sup>th</sup> percentile velocity from the cumulative distribution function (CDF) of the resulting outflow model (Shaban et al. 2023).

The wavelength ranges of KCWI and MUSE provide mutual coverage of several Fe II transitions. We simultaneously fit a two kinematic component outflow model to Fe II 2344, 2374, 2382, 2586 and 2600 absorption lines along with five Fe II emission lines as described in §3.1 and Table 2. The best fit outflow model (orange line) and 300 realizations of the outflow model (gray lines) created by randomly sampling the posterior distribution are presented in Figure 8.

Given the relatively small oscillator strengths ( $f_0$ ) of the Fe II 2344, 2374, and 2586 absorption transitions in the spectrum of G1, these lines provide more reliable column density estimates compared to the higher- $f_0$  Fe II transitions or the saturated Mg II doublet. However, due to the limited resolution of MUSE and KCWI ( $R \sim 2000 - 3000$ ), we consider these column densities to be lower limits. From the posterior distribution of the model parameters, we measure the absorption weighted mean outflow velocity traced by Fe II absorption as  $V_{out} = -122^{+8}_{-8}$  km s<sup>-1</sup>. The total Fe II absorption column density is  $\log(N_{out}/\text{cm}^{-2}) = 15.82^{+0.16}_{-0.23}$ . This corresponds to a rest frame equivalent width of the Fe II

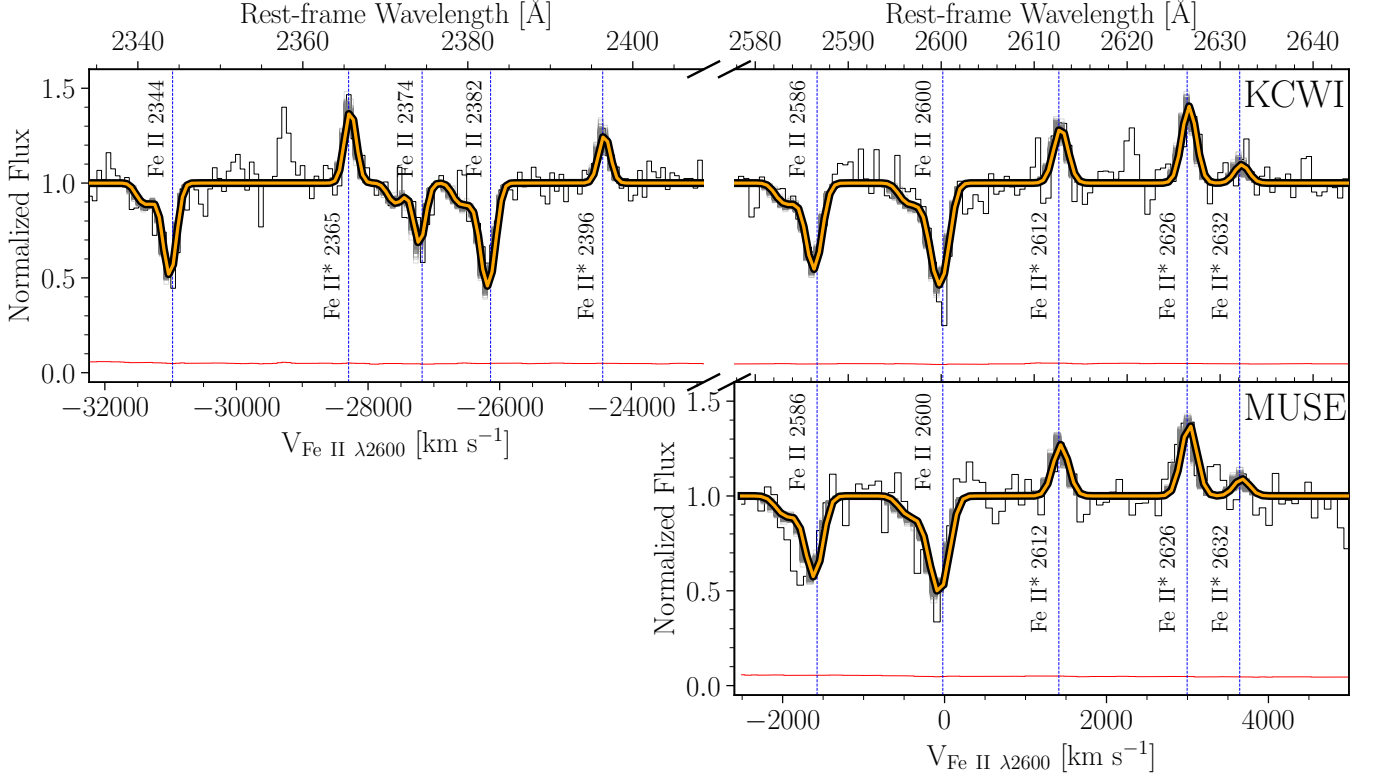


**Figure 8.** Galactic outflow kinematics traced by Fe II transitions in galaxy G1 from KCWI (*top row*) and MUSE (*bottom panel*), respectively. All velocities are set to zero with respect to the rest-frame wavelength of Fe II  $\lambda 2600$  at G1’s systemic redshift. The solid black and red lines represent the normalized flux and uncertainty. The solid orange line represents the best fit outflow model. The faint gray lines represent 300 random realizations from the posterior distribution. All the absorption/emission features are marked with dashed vertical blue lines. We observe only five Fe II transitions lines in the MUSE spectrum because the MUSE wavelength coverage starts at  $\lambda_{obs} \approx 4600 \text{ \AA}$  ( $\lambda_{rest} \approx 2576 \text{ \AA}$ ) (see Table 2 for more details).

$\lambda 2382$  line of  $W_r = 1.58 \pm 0.05 \text{ \AA}$ . The gas covering fraction of the first kinematic component is  $C_{f,1} = 0.59^{+0.03}_{-0.03}$  and the second component is  $C_{f,2} = 0.12 \pm 0.01$ , respectively. Similar to the Mg II absorption, the gas covering fraction of the high velocity second component is smaller than the first component. Both the Mg II and Fe II absorption trace the cool  $10^4 \text{ K}$  outflowing gas and the highest velocity parts of the outflow is optically thin with very low covering fraction. The maximum 95<sup>th</sup> percentile outflow velocity traced by the Fe II 2382 is  $V_{95} = -504^{+23}_{-24} \text{ km s}^{-1}$ . The measured outflow kinematics and column densities of the Fe II and Mg II absorption are summarized in Table 3.

We use the measured outflow gas column density  $N$ , covering fraction  $C_f$ , and mean outflow velocity  $V_{out}$  to quantify the mass outflow rate ( $\dot{M}_{out}$ ) from galaxy G1. Assuming a thin spherical shell geometry,  $\dot{M}_{out}$  can be

written as (see Shaban et al. (2023) for derivation):

$$\dot{M}_{out} \gtrsim 22 M_{\odot} \text{ yr}^{-1} \frac{C_f}{1.0} \frac{\Omega_w}{4\pi} \frac{V_{out}}{300 \text{ km s}^{-1}} \frac{N_H}{10^{20} \text{ cm}^{-2}} \frac{R}{5 \text{ kpc}}, \quad (8)$$

where  $N_H$  is the Hydrogen column density, and  $R$  is the radius of the outflow. We use the absorption weighted mean outflow velocity  $V_{out}$  and use the mean absorption weighted gas covering fraction of the two kinematic components as the covering fraction of the outflowing gas  $C_f$ . We calculate the total gas column density  $N_H$  from the total column densities of Fe II and Mg II. To perform this conversion, we assume no-ionization correction, and use the mean metallicity of galaxy G1 as the metallicity of the outflowing gas (§4.1). We also use dust depletion of -1.3 dex and -1.0 dex for Mg II and Fe II, respectively, (Jenkins 2009) and assume solar abundances from Lodders (2003).

The radius  $R$  of the outflow is one of the least constrained quantities in the calculation of  $\dot{M}_{out}$ . Since we do not detect any Mg II emission above the noise level, we assume a conservative estimate of the mean radius of the outflow to be  $R = 5 \text{ kpc}$  (see the appendix of

**Table 3.** Measured outflow properties from the Fe II and Mg II transitions of the galaxy G1: (2) is the rest-frame equivalent width, (3) is the mean outflow velocity, (4) is the 95<sup>th</sup> percentile outflow velocity, (5) and (6) are the column density of the first and second outflow components, (7) and (8) are the covering fractions for the first and second outflow components, and (9) is the measured mass outflow rate.

Species	$W_{r,out}^a$ [Å]	$V_{out}^a$ [km s <sup>-1</sup> ]	$V_{95}^a$ [km s <sup>-1</sup> ]	$\log_{10}(N_1/\text{cm}^{-2})$	$\log_{10}(N_2/\text{cm}^{-2})$	$C_{f,1}$	$C_{f,2}$	$\dot{M}_{out}$ [ $M_{\odot} \text{ yr}^{-1}$ ]
(1)	(2)	(3)	(4)	(5)	(6)	(7)	(8)	(9)
Fe II	$1.58_{-0.05}^{+0.05}$	$-121_{-8}^{+7}$	$-504_{-24}^{+23}$	$15.01_{-0.08}^{+0.10}$	$15.74_{-0.30}^{+0.19}$	$0.59_{-0.03}^{+0.03}$	$0.12_{-0.01}^{+0.01}$	$64_{-27}^{+31}$
Mg II	$1.97_{-0.06}^{+0.06}$	$-179_{-4}^{+5}$	$-415_{-7}^{+10}$	$15.19_{-0.55}^{+0.57}$	$15.60_{-0.52}^{+0.29}$	$0.74_{-0.03}^{+0.06}$	$0.41_{-0.03}^{+0.03}$	$248_{-147}^{+170}$

<sup>a</sup>Both quantities are measured for the lines with the highest oscillator strength Fe II  $\lambda 2382$  and Mg II  $\lambda 2796$ .

Shaban et al. 2023). At this radius, we get an estimate of the mass outflow rate for the galaxy at  $z = 0.785273$  to be  $\dot{M}_{out}(R = 5 \text{ kpc}) \gtrsim 248_{-147}^{+170} M_{\odot} \text{ yr}^{-1}$  using Mg II measurements. This high uncertainty on the value of  $\dot{M}_{out}$  is due to the fact that the Mg II lines are saturated. This leads to high uncertainty on column density that gets propagated to the value of  $\dot{M}_{out}$ .

Given that, we detect optically thin Fe II lines that better constrain the column density of the outflowing gas. We measure the mass outflow rate of G1 at 5 kpc to be  $\dot{M}_{out}(R = 5 \text{ kpc}) \gtrsim 64_{-27}^{+31} M_{\odot} \text{ yr}^{-1}$ . Given all these assumptions, our estimates on  $\dot{M}_{out}$  are lower limits. In reality, the total mass outflow will be higher than our estimates because we are only accounting for the cool phase  $10^4 K$  gas that is traced by Fe II and Mg II.

By comparing this mass outflow rate from Fe II to the SFR from H $\beta$  (see §3.3.1) of the galaxy G1, we constrain the mass loading factor ( $\eta = \dot{M}_{out}/SFR$ ) to be  $\eta \gtrsim 2.1_{-0.9}^{+1.0}$ .

#### 4.3. CGM Measurements

In this section, we report the variation of Mg II absorption strengths in the CGM of galaxy G1. The CGM is sampled six times by six lines of sight towards the background arc SGAS1527 between 54 and 66 kpc.

Figure 9 shows the Mg II absorption detected along the six sightlines towards the background arc. Each Mg II absorption doublet is fitted with a double Gaussian, and the best fit model (thick orange lines) and the corresponding 300 model realizations (light orange lines) created by randomly sampling the model posterior distribution are presented. The Mg II 2796 absorption equivalent width ( $W_r$ ) is computed by integrating the best fit model along each line of sight. Individual Mg II absorption strengths are presented in each panel of Figure 9.

Since each sightline intersects the galaxy’s CGM at different impact parameters, we compute the variation in CGM absorption strengths between 54 and 66 kpc of

galaxy G1. These measurements are presented in Figure 10, panel (a). Individual absorption strengths vary by a factor of 2.2 between 0.29 Å to 0.64 Å within 10 kpc of each other. The mean absorption strength is  $\langle W_r \rangle = 0.4 \text{ Å}$  at  $\langle D \rangle = 60 \text{ kpc}$ . In addition, the centroid velocities of Mg II from the model fits for the arc sightlines do not follow G1’s disk kinematics and are scattered around the zero-systemic velocity (see Appendix A).

As sightline to sightline variations are in the halo of the same galaxy, we quantify the small scale variation of Mg II absorption in the CGM of a single galaxy. We measure the pairwise fractional difference ( $\Delta W$ ) in rest-frame equivalent width between two sightlines ( $i, j$ ) as:

$$\Delta W_{i,j} = \frac{W_{r,i} - W_{r,j}}{W_{r,i}}, \quad (9)$$

where  $W_{r,i} \geq W_{r,j}$  (Ellison et al. 2004). Figure 10, panel (b), shows  $\Delta W$  as a function of physical separation between two sightlines. A value of  $\Delta W = 1$  implies that two sightlines are 100% different (i.e., the CGM is highly in-homogeneous), while  $\Delta W = 0$  implies a fully homogeneous CGM. We observe  $\Delta W \approx 0.25$  at a separation of  $< 0.5 \text{ kpc}$  and decreases at 1 kpc to 0.15. This is followed by an increase up to 0.5 in the  $\Delta W$  at  $\approx 2 \text{ kpc}$ . We see similar variations at separations of  $\Delta d = 7.5 - 10 \text{ kpc}$ . This indicates the existence of small scale structure in the CGM of the galaxy. Indeed, studies of Mg II absorbers using high resolution spectra suggests individual cloud sizes of 100s of parsecs (Rauch et al. 2002).

All the  $\Delta W$  values at different separations are  $\lesssim 0.56$ . This suggests that on kpc scales, Mg II absorption in this CGM is spatially coherent.

We quantify the large scale spatial coherence of Mg II absorption as follows. The Mg II fractional difference as a function of  $\Delta d$  can be characterized as:

$$f(\Delta d) = \begin{cases} \delta & ; \text{ if } \Delta d < r_{coh} \\ \delta \left( \frac{\Delta d}{r_{coh}} \right)^{\gamma} & ; \text{ if } \Delta d \geq r_{coh} \end{cases} \quad (10)$$

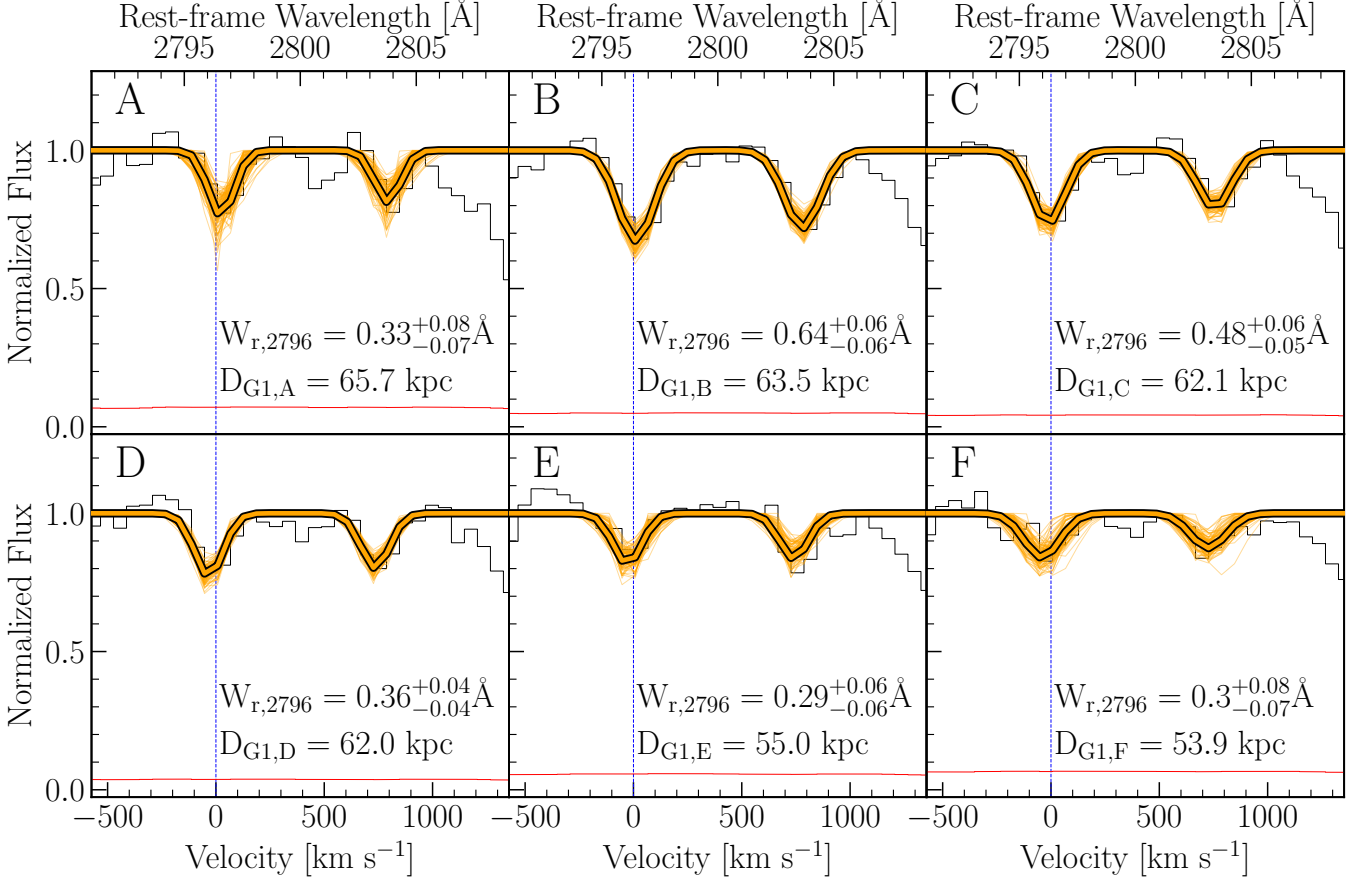


**Figure 9.** The Mg II 2796, 2803 Å absorption in the CGM of the galaxy G1 along 6 sightlines probed by the arc from KCWI as shown in Figure 2. Velocities are centered on the Mg II 2796 transition at the systemic redshift of galaxy G1, marked as blue dashed line. The best fit models for Mg II doublet (orange line) and the Mg II 2796 rest-frame equivalent width ( $W_r$ ) for each aperture is shown. The faint orange lines are 100 random realizations of the model from the PPDF resulting from `emcee` runs.

where  $\delta$  is the amplitude of  $\Delta W$  at  $\Delta d \leq r_{coh}$ , and  $r_{coh}$  is the coherence length scale, and  $\gamma$  is the index of the power-law for  $\Delta d \geq r_{coh}$ .

This model is fitted to the observations presented in Figure 10, panel (b), which yields an amplitude of  $\delta = 0.07^{+0.01}_{-0.01}$ ,  $\gamma = 0.69^{+0.23}_{-0.22}$ , and a coherence length scale of  $r_{coh} = 2.73^{+1.08}_{-1.59}$  kpc, respectively. This coherence length value is consistent with the size of the complex gaseous structures sizes of  $1.4 \text{ kpc} \leq l \leq 7.8 \text{ kpc}$  that are reported in Afruni et al. (2023), which is also from lensed arcs tomography of foreground systems. Since galaxy G1 is driving strong galactic outflow ( $V_{out} = -179 \text{ km s}^{-1}$ ), it is plausible that the background sightlines are tracing a bulk flow of outflowing gas in the CGM. This might explain the large and coherent CGM structure observed.

Assuming that the CGM gas is originating from the strong galactic outflow of G1, these observations can be reported as a radial profile of the CGM. Figure 10, panel (c), shows all the measurements as a function of impact

parameter from galaxy G1 (cyan diamonds). At  $D = 1$  kpc the outflow absorption down-the-barrel strength of G1 is reported. Clearly, the Mg II absorption strength decreases as we move from  $D = 1$  kpc to  $D = 50$  kpc. This radial drop-off is similar to the statistical CGM observations of 182 galaxies at  $0.07 \leq z \leq 1.1$  in the MAGICAT survey (red circles) from Nielsen et al. (2013b) and the low impact parameter observations (green squares) from Kacprzak et al. (2013), and measurements from the stacked spectra in bins of impact parameters of galaxies (blue circles) from Bordoloi et al. (2011).

The Mg II absorption radial profile around a single galaxy is broadly consistent with the average radial absorption profile around a large sample of galaxies at similar redshifts. However, the scatter observed in the CGM of a single galaxy ( $\sigma(W_r) = 0.13$ ) is much smaller than that observed around the MAGICAT galaxies. This suggests that such statistical samples have additional degrees of freedom (e.g., stellar/halo mass, star-formation

rate, azimuthal angle) that contribute to the large scatter in them (Fernandez-Figueroa et al. 2022; Afruni et al. 2023). Studying the CGM of individual galaxies can reduce many of these uncertainties, allowing a more controlled experiment. This work highlights the power of gravitational lensing in probing the faint CGM of foreground galaxies in a spatially resolved manner at multiple sightlines compared to the pencil beam background quasar sightlines that provide just one measurement per sightline per galaxy.

If the observed CGM of galaxy G1 originates from entrained gas carried out to the CGM by a strong outflow, we can calculate an approximate timescale of the event. Assuming a constant velocity ( $V_{out} = 179 \text{ km s}^{-1}$ ) of the Mg II tracing the outflow, it will require  $\approx 328 \text{ Myr}$  for the outflow to reach an impact parameter of  $D \sim 60 \text{ kpc}$ .

Recently, it has become increasingly feasible to use strong gravitational lensing to probe the CGM of individual galaxies. (Lopez et al. 2020; Tejos et al. 2021; Fernandez-Figueroa et al. 2022; Bordoloi et al. 2022).

Rubin et al. (2018) report a coherence length scales of  $\sim 8 - 22 \text{ kpc}$  from the Mg II absorption in 8 foreground absorbing systems probed by a background quadruply lensed quasar at  $z = 2.38$  with KCWI. Augustin et al. (2021) used a MUSE observation of a quadruply lensed quasar to probe two absorbing Mg II systems at  $z \approx 1.2$  and  $z \approx 1.4$  and measured coherence length scales of  $\sim 5\text{-}6 \text{ kpc}$  possibly corresponding to inflowing filaments in the first system, and  $\leq 2 \text{ kpc}$  corresponding to outflowing clumpy structures in the second system. Dutta et al. (2024) calculate a coherence length scale of  $10 \text{ kpc}$  in the CGM of foreground individual galaxies, groups (more than 1 galaxy according to their definition), and absorbing systems with  $z \sim 0.5 - 2$  using two fields background lensed quasars at  $z \approx 2.2$  and  $2.8$  with MUSE observations. Furthermore, they report that high-ionization C IV gas is more coherent than the low-ionization Mg II gas. This is an indication of the clumpy nature of the Mg II gas. In addition, Afruni et al. (2023) showed that C IV is clumpy on kpc scales, and reported a coherence length scale in the range of  $1.4 - 7.8 \text{ kpc}$  using the arc tomography technique (Lopez et al. 2018) from a sample of gravitationally lensed galaxies probing absorbing systems at  $z \approx 1$ . In panel *d*, Figure 10, we compare Mg II measurements of G1 with the measurements of Mg II absorption using the gravitational-arc tomography (ARCTOMO; PI: S. Lopez) from Lopez et al. (2018), Lopez et al. (2020), Tejos et al. (2021), and Afruni et al. (2023). G1 Mg II measurements shows a consistent trend with the ARCTOMO data.

One should note that the background sightlines used in this work are spatially extended (unlike pencil beam quasar sightlines). Spatially extended background sightlines in themselves will only have spatially averaged absorption measurements which will smear out information regarding small scale gas structure and covering fraction of the gas (see e.g., Bordoloi et al. 2011, 2014a, for discussions on this topic). Therefore, it becomes inherently difficult to study small-scale cloud properties using spatially extended background sources. Further, as  $r_{coh}$  may vary between different galaxies/CGM; it is advisable to measure  $r_{coh}$  independently in individual CGM of galaxies. This might be reflected in the wide range of gas coherence lengths reported in the literature. In future work, this technique will be extended to a large sample of spatially resolved CGM observations, which will enable the study of gas coherence lengths in different galaxy types and environments.

## 5. CONCLUSIONS

This work uses observations from Keck/KCWI and VLT/MUSE wide field IFU spectrographs in the field of view of a bright gravitationally lensed galaxy at  $z \approx 2.76$ . The field has a galaxy at  $z \approx 0.8$ , G1, and Mg II absorption is detected in its CGM using the gravitationally lensed galaxy as a background source. This work analyzes both the down-the-barrel spectroscopy of the foreground galaxy and the spectra of the background source. The main conclusions of this work are as follows:

- The foreground  $z \approx 0.8$  galaxy G1 hosts an extended emission gas halo beyond the stellar disk of the galaxy, traced by [O II], [O III], and H $\beta$  emission lines. This halo is spatially extended with a maximum diameter of  $33.4 \text{ kpc}$  in the plane of G1 at  $z = 0.8$  as measured from the [O II] emission (Figure 4).
- The [O II], [O III], and H $\beta$  emission maps show a velocity gradient consistent with the kinematic signature of a co-rotating gas halo (Figure 5).
- From the emission lines [O II], [O III], and H $\beta$  fluxes, we measure the metallicity of the extended emission gas halo to be  $12 + \log(\text{O}/\text{H}) = 8.99 \pm 0.04$ , which is  $3_{-1}^{+1}\%$  greater than the photospheric solar value (Figure 6).
- G1 is driving a strong galactic outflow traced by blueshifted Mg II and Fe II absorption lines. The mean outflow velocity is measured to be  $\approx -179 \text{ km s}^{-1}$  and  $\approx -122 \text{ km s}^{-1}$  from Mg II and

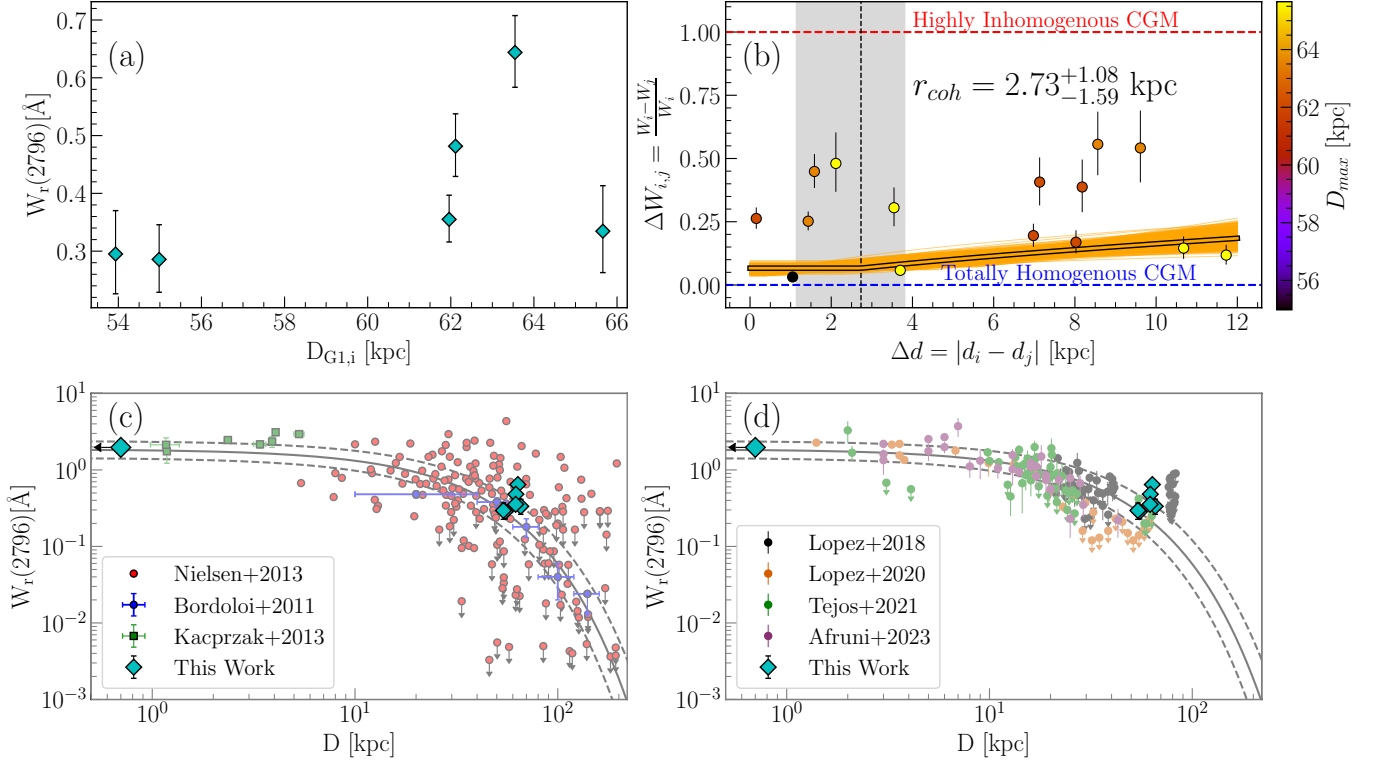


**Figure 10.** *Panel (a):* The rest-frame equivalent width  $W_r$  of the Mg II 2796 absorption line at the redshift of the G1 at the sightlines along the arc in Figure 2 only versus the impact parameter between G1 and these sightlines. *Panel (b):* The fractional difference (equation 9) of  $W_r$  of Mg II 2796 from the left panel versus the separation between each pair of sightlines  $(i, j)$ . The color-bar represents the sightline with the maximum impact parameter from the galaxy for each pair of sightlines  $(i, j)$ . The solid dark orange line is the fractional difference model (equation 9) fit for the data. The vertical black dashed line represents the median value of the coherence length  $r_{coh} = 2.73$  kpc, and the gray band around it represents the range of  $r_{coh}$  values between the 16<sup>th</sup> and 84<sup>th</sup> percentiles of its posterior distribution. The faint orange lines are 300 model realizations from the posterior distribution of the model parameters. *Panel (c):* The rest-frame equivalent width  $W_r$  of the Mg II 2796 versus impact parameter from the galaxy. The cyan diamonds are the measurements from G1 with the leftmost point is the  $W_r$  from the outflow in G1, and the rest of the cyan diamonds are from the positions across the arc at  $\sim 60$  kpc. The blue data points are from the stacked spectra in distance bins from Bordoloi et al. (2011). The green data points are from Kacprzak et al. (2013) for 7 galaxies at  $z \sim 0.1$ . The red data points are from Nielsen et al. (2013b) of 182 galaxies at  $0.07 \leq z \leq 1.1$ . The solid line is the log-linear relation fit from Nielsen et al. (2013a) for  $\log_{10}(W_r) = \alpha_1 D + \alpha_2$ , where  $\alpha_1 = -0.015 \pm 0.002$  and  $\alpha_2 = 0.26 \pm 0.11$ . The two dashed black lines capture the  $1\sigma$  bounds on the fit. *Panel (d):* We compare our measurements to gravitational-arc tomography (ARCTOMO) data from Lopez et al. (2018) (black circles), Lopez et al. (2020) (orange circles), Tejos et al. (2021) (green circles), and Afruni et al. (2023) (purple circles). The solid and dashed black lines are the same as Panel (c).

Fe II absorption lines, respectively (Figures 7 and 8).

- The mass outflow rate for G1 at radius of  $R = 5$  kpc is  $\dot{M}_{out} \geq 64^{+31}_{-27} M_{\odot} \text{ yr}^{-1}$  as measured from the optically thin Fe II absorption lines (Figure 7), corresponding to a mass loading factor of  $\eta \geq 2.1^{+1.0}_{-0.9}$ .
- Using the lensed arc of background galaxy at  $z = 2.76$ , we detect the Mg II doublet tracing the outflow up to distances of 54–66 kpc away from G1 (Figures 2 and 9).

- We see small scale variations in the rest-frame equivalent width of the Mg II ionized gas tracing the outflow in the CGM of G1 at impact parameter  $\approx 60$  kpc, within a region of size of 12 kpc (Figures 9 and 10).
- By using a power-law model to fit the fractional difference measurements, we obtain a coherence length scale of the CGM of  $2.73^{+1.08}_{-1.59}$  kpc (§4.3 and Figure 10).

In conclusion, a galaxy at  $z \approx 0.8$  is driving a strong galactic outflow, which has a high metallicity co-rotating gas halo extending out to a maximum radius of 16.7 kpc in the plane of G1. The CGM of this galaxy G1 shows

Mg II absorption that extends out to an impact parameter of 66 kpc in the plane of G1. The CGM absorption is spatially coherent at large scales, with coherence length of 2.7 kpc. These observations taken together suggest that we may be observing a galaxy, where the galactic outflow is getting recycled, and enriched recycled outflow might be co-rotating around the galaxy before forming the next generation of stars in the galaxy. This scenario is consistent with what is expected in galaxy formation simulations.

This work shows how gravitational lensing, as a cosmic telescope, can be coupled with IFU instruments to probe the small scale variations in the faint CGM of foreground galaxies. The measurements of such variations will provide strong constraints for galaxy formation and evolution models.

## 6. ACKNOWLEDGMENTS

This material is based upon work supported by the National Science Foundation under grant number: NSF AST-2206853. Some data presented herein were obtained at Keck Observatory, which is a private 501(c)3 non-profit organization operated as a scientific partnership among the California Institute of Technology, the University of California, and the National Aeronautics and Space Administration. The Observatory was made possible by the generous financial support of the W. M. Keck Foundation. The authors wish to recognize and

acknowledge the very significant cultural role and reverence that the summit of Mauna Kea has always had within the Native Hawaiian community. We are most fortunate to have the opportunity to conduct observations from this mountain. This work is based on observations collected at the European Organization for Astronomical Research in the Southern Hemisphere under ESO program 0103.A-0485(B). This research made use of Montage. It is funded by the National Science Foundation under Grant Number ACI-1440620, and was previously funded by the National Aeronautics and Space Administration's Earth Science Technology Office, Computation Technologies Project, under Cooperative Agreement Number NCC5-626 between NASA and the California Institute of Technology. Furthermore, we used observations made with the NASA/ESA Hubble Space Telescope, obtained from the data archive at the Space Telescope Science Institute (STScI). STScI is operated by the Association of Universities for Research in Astronomy, Inc. under NASA contract NAS 5-26555. N.T. and S.L. acknowledge support by FONDECYT grant 1231187. All the *HST* data used in this paper can be found in MAST: [10.17909/jgas-n891](https://mast.stsci.org/#/jgas-n891).

*Facilities:* HST(WFC3), Keck:II (KCWI), VLT (MUSE).

*Software:* [astropy \(Astropy Collaboration et al. 2013, 2018, 2022\)](#), [photutils \(Bradley et al. 2023\)](#)

## APPENDIX

### A. CGM GAS IS NOT CO-ROTATING WITH THE STELLAR DISK OF G1

In this appendix, we calculate the impact parameter of each spaxel with [O II] emission within the stellar disk of G1 (green contour in Figure 11). Any pixel with x-position to the left of the central pixel of G1 is assigned a negative impact parameter. Figure 11 shows the kinematics of the stellar disk of G1 as traced by the [O II] emission lines (blue circles). In addition, we plot the centroid velocities of Mg II absorption for the six apertures across the arc. The Mg II velocities show both positive and negative values with respect to the systemic redshift of G1. Particularly, the closest apertures show velocities that are not aligned with the kinematics of the stellar disk of the galaxy. This suggests that the Mg II absorption is not co-rotating with the disk of G1 (green contour in Figure 11). This further supports that the origin of this gas is due to galactic outflow from G1.

## REFERENCES

- Afruni, A., Lopez, S., Anshul, P., et al. 2023, *A&A*, 680, A112, doi: [10.1051/0004-6361/202347867](https://doi.org/10.1051/0004-6361/202347867)
- Asplund, M., Amarsi, A. M., & Grevesse, N. 2021, *A&A*, 653, A141, doi: [10.1051/0004-6361/202140445](https://doi.org/10.1051/0004-6361/202140445)
- Astropy Collaboration, Robitaille, T. P., Tollerud, E. J., et al. 2013, *A&A*, 558, A33, doi: [10.1051/0004-6361/201322068](https://doi.org/10.1051/0004-6361/201322068)
- Astropy Collaboration, Price-Whelan, A. M., Sipőcz, B. M., et al. 2018, *AJ*, 156, 123, doi: [10.3847/1538-3881/aabc4f](https://doi.org/10.3847/1538-3881/aabc4f)
- Astropy Collaboration, Price-Whelan, A. M., Lim, P. L., et al. 2022, *ApJ*, 935, 167, doi: [10.3847/1538-4357/ac7c74](https://doi.org/10.3847/1538-4357/ac7c74)
- Augustin, R., Péroux, C., Hamanowicz, A., et al. 2021, *MNRAS*, 505, 6195, doi: [10.1093/mnras/stab1673](https://doi.org/10.1093/mnras/stab1673)

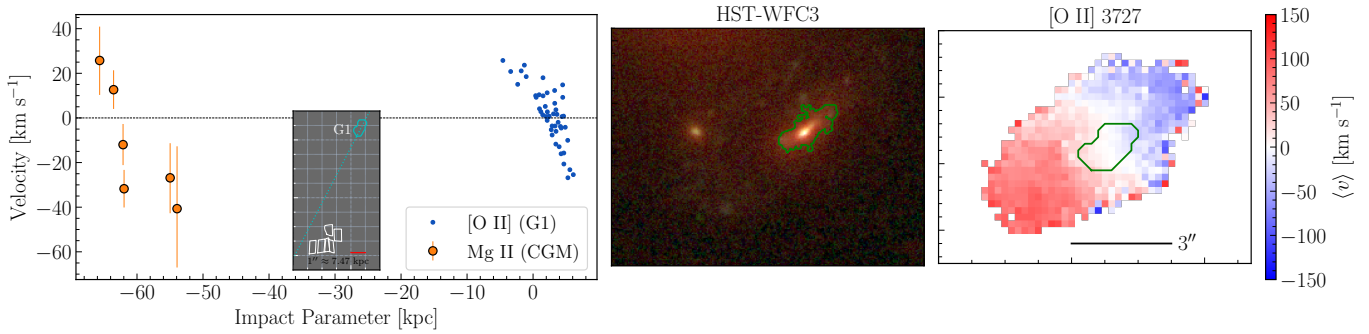


**Figure 11.** *Left:* G1 kinematics as traced by the [O II] emission lines (blue circles). The orange data points represent the velocity centroids of Mg II absorption lines with respect to the galaxy systemic redshift. The inset shows the ray-traced positions of G1 and the background lines of sight in the absorber plane of G1. The dotted cyan line in the inset marks the major axis of G1, extended out to 60 kpc. *Middle:* HST RGB image of the galaxy G1, with the green contour marking the  $3\sigma$  isophotes of stellar light of the galaxy from the WFC3-UVIS F606W filter. *Right:* 2D velocity map of the [O II] emission from Figure 5. The green contour represents the location of the stellar light of the galaxy from the HST image in the middle panel. This Figure qualitatively shows that the Mg II absorption in the CGM of G1 is not co-rotating with the stellar disk. The  $3''$  black line marker corresponds to  $\approx 10$  kpc in the plane of G1.

- Bacon, R., Accardo, M., Adjali, L., et al. 2010, in Society of Photo-Optical Instrumentation Engineers (SPIE) Conference Series, Vol. 7735, Ground-based and Airborne Instrumentation for Astronomy III, ed. I. S. McLean, S. K. Ramsay, & H. Takami, 773508, doi: [10.1117/12.856027](https://doi.org/10.1117/12.856027)
- Bayliss, M. B., Hennawi, J. F., Gladders, M. D., et al. 2011, ApJS, 193, 8, doi: [10.1088/0067-0049/193/1/8](https://doi.org/10.1088/0067-0049/193/1/8)
- Behroozi, P., Wechsler, R. H., Hearin, A. P., & Conroy, C. 2019, MNRAS, 488, 3143, doi: [10.1093/mnras/stz1182](https://doi.org/10.1093/mnras/stz1182)
- Berg, T. A. M., Afruni, A., Ledoux, C., et al. 2024, arXiv e-prints, arXiv:2412.07652, doi: [10.48550/arXiv.2412.07652](https://doi.org/10.48550/arXiv.2412.07652)
- Bielby, R. M., Stott, J. P., Cullen, F., et al. 2019, MNRAS, 486, 21, doi: [10.1093/mnras/stz774](https://doi.org/10.1093/mnras/stz774)
- Bordoloi, R., Lilly, S. J., Kacprzak, G. G., & Churchill, C. W. 2014a, ApJ, 784, 108, doi: [10.1088/0004-637X/784/2/108](https://doi.org/10.1088/0004-637X/784/2/108)
- Bordoloi, R., Rigby, J. R., Tumlinson, J., et al. 2016, MNRAS, 458, 1891, doi: [10.1093/mnras/stw449](https://doi.org/10.1093/mnras/stw449)
- Bordoloi, R., Lilly, S. J., Knobel, C., et al. 2011, ApJ, 743, 10, doi: [10.1088/0004-637X/743/1/10](https://doi.org/10.1088/0004-637X/743/1/10)
- Bordoloi, R., Lilly, S. J., Hardmeier, E., et al. 2014b, ApJ, 794, 130, doi: [10.1088/0004-637X/794/2/130](https://doi.org/10.1088/0004-637X/794/2/130)
- Bordoloi, R., O'Meara, J. M., Sharon, K., et al. 2022, Nature, 606, 59, doi: [10.1038/s41586-022-04616-1](https://doi.org/10.1038/s41586-022-04616-1)
- Bordoloi, R., Simcoe, R. A., Matthee, J., et al. 2024, ApJ, 963, 28, doi: [10.3847/1538-4357/ad1b63](https://doi.org/10.3847/1538-4357/ad1b63)
- Bradley, L., Sipőcz, B., Robitaille, T., et al. 2023, astropy/photutils: 1.8.0, 1.8.0, Zenodo, doi: [10.5281/zenodo.7946442](https://doi.org/10.5281/zenodo.7946442)
- Burchett, J. N., Rubin, K. H. R., Prochaska, J. X., et al. 2021, ApJ, 909, 151, doi: [10.3847/1538-4357/abd4e0](https://doi.org/10.3847/1538-4357/abd4e0)
- Calzetti, D., Armus, L., Bohlin, R. C., et al. 2000, ApJ, 533, 682, doi: [10.1086/308692](https://doi.org/10.1086/308692)
- Cardelli, J. A., Clayton, G. C., & Mathis, J. S. 1989, ApJ, 345, 245, doi: [10.1086/167900](https://doi.org/10.1086/167900)
- Chambers, K. C., Magnier, E. A., Metcalfe, N., et al. 2016, arXiv e-prints, arXiv:1612.05560, doi: [10.48550/arXiv.1612.05560](https://doi.org/10.48550/arXiv.1612.05560)
- Chen, Y.-M., Tremonti, C. A., Heckman, T. M., et al. 2010, AJ, 140, 445, doi: [10.1088/0004-6256/140/2/445](https://doi.org/10.1088/0004-6256/140/2/445)
- Chisholm, J., Bordoloi, R., Rigby, J. R., & Bayliss, M. 2018, MNRAS, 474, 1688, doi: [10.1093/mnras/stx2848](https://doi.org/10.1093/mnras/stx2848)
- Chisholm, J., Tremonti, C. A., Leitherer, C., Chen, Y., & Wofford, A. 2016, MNRAS, 457, 3133, doi: [10.1093/mnras/stw178](https://doi.org/10.1093/mnras/stw178)
- Chisholm, J., Tremonti, C. A., Leitherer, C., et al. 2015, ApJ, 811, 149, doi: [10.1088/0004-637X/811/2/149](https://doi.org/10.1088/0004-637X/811/2/149)
- Clark, S., Bordoloi, R., & Fox, A. J. 2022, MNRAS, 512, 811, doi: [10.1093/mnras/stac504](https://doi.org/10.1093/mnras/stac504)
- Conroy, C., & Gunn, J. E. 2010, ApJ, 712, 833, doi: [10.1088/0004-637X/712/2/833](https://doi.org/10.1088/0004-637X/712/2/833)
- Conroy, C., Gunn, J. E., & White, M. 2009, ApJ, 699, 486, doi: [10.1088/0004-637X/699/1/486](https://doi.org/10.1088/0004-637X/699/1/486)
- Doi, M., Tanaka, M., Fukugita, M., et al. 2010, AJ, 139, 1628, doi: [10.1088/0004-6256/139/4/1628](https://doi.org/10.1088/0004-6256/139/4/1628)
- Draine, B. T. 2011, Physics of the Interstellar and Intergalactic Medium (Princeton University Press)
- Dutta, R., Acebron, A., Fumagalli, M., et al. 2024, MNRAS, doi: [10.1093/mnras/stae048](https://doi.org/10.1093/mnras/stae048)
- Dutta, R., Fossati, M., Fumagalli, M., et al. 2023, MNRAS, doi: [10.1093/mnras/stad1002](https://doi.org/10.1093/mnras/stad1002)

- Ellison, S. L., Ibata, R., Pettini, M., et al. 2004, *A&A*, 414, 79, doi: [10.1051/0004-6361:20034003](https://doi.org/10.1051/0004-6361:20034003)
- Faucher-Giguère, C.-A., & Oh, S. P. 2023, *ARA&A*, 61, 131, doi: [10.1146/annurev-astro-052920-125203](https://doi.org/10.1146/annurev-astro-052920-125203)
- Fernandez-Figueroa, A., Lopez, S., Tejos, N., et al. 2022, *MNRAS*, 517, 2214, doi: [10.1093/mnras/stac2851](https://doi.org/10.1093/mnras/stac2851)
- Fitzpatrick, E. L. 1999, *PASP*, 111, 63, doi: [10.1086/316293](https://doi.org/10.1086/316293)
- Fluetsch, A., Maiolino, R., Carniani, S., et al. 2021, *MNRAS*, 505, 5753, doi: [10.1093/mnras/stab1666](https://doi.org/10.1093/mnras/stab1666)
- Foreman-Mackey, D., Hogg, D. W., Lang, D., & Goodman, J. 2013, *PASP*, 125, 306, doi: [10.1086/670067](https://doi.org/10.1086/670067)
- Fox, A. J., Richter, P., Ashley, T., et al. 2019, *ApJ*, 884, 53, doi: [10.3847/1538-4357/ab40ad](https://doi.org/10.3847/1538-4357/ab40ad)
- Fukugita, M., Ichikawa, T., Gunn, J. E., et al. 1996, *AJ*, 111, 1748, doi: [10.1086/117915](https://doi.org/10.1086/117915)
- Hafen, Z., Faucher-Giguère, C.-A., Anglés-Alcázar, D., et al. 2019, *MNRAS*, 488, 1248, doi: [10.1093/mnras/stz1773](https://doi.org/10.1093/mnras/stz1773)
- Heckman, T. M., Alexandroff, R. M., Borthakur, S., Overzier, R., & Leitherer, C. 2015, *ApJ*, 809, 147, doi: [10.1088/0004-637X/809/2/147](https://doi.org/10.1088/0004-637X/809/2/147)
- Heckman, T. M., Lehnert, M. D., Strickland, D. K., & Armus, L. 2000, *ApJS*, 129, 493, doi: [10.1086/313421](https://doi.org/10.1086/313421)
- Ho, S. H., Martin, C. L., Kacprzak, G. G., & Churchill, C. W. 2017, *ApJ*, 835, 267, doi: [10.3847/1538-4357/835/2/267](https://doi.org/10.3847/1538-4357/835/2/267)
- Hogg, D. W. 1999, arXiv e-prints, astro. <https://arxiv.org/abs/astro-ph/9905116>
- Hopkins, P. F., Kereš, D., Oñorbe, J., et al. 2014, *MNRAS*, 445, 581, doi: [10.1093/mnras/stu1738](https://doi.org/10.1093/mnras/stu1738)
- Hopkins, P. F., Murray, N., Quataert, E., & Thompson, T. A. 2010, *MNRAS*, 401, L19, doi: [10.1111/j.1745-3933.2009.00777.x](https://doi.org/10.1111/j.1745-3933.2009.00777.x)
- Hopkins, P. F., Quataert, E., & Murray, N. 2012, *MNRAS*, 421, 3522, doi: [10.1111/j.1365-2966.2012.20593.x](https://doi.org/10.1111/j.1365-2966.2012.20593.x)
- Jacob, J. C., Katz, D. S., Berriman, G. B., et al. 2010a, arXiv e-prints, arXiv:1005.4454, doi: [10.48550/arXiv.1005.4454](https://doi.org/10.48550/arXiv.1005.4454)
- . 2010b, Montage: An Astronomical Image Mosaicking Toolkit, Astrophysics Source Code Library, record ascl:1010.036
- Jenkins, E. B. 2009, *ApJ*, 700, 1299, doi: [10.1088/0004-637X/700/2/1299](https://doi.org/10.1088/0004-637X/700/2/1299)
- Johnson, B., Foreman-Mackey, D., Sick, J., et al. 2023, *dfm/python-fsps: v0.4.6, v0.4.6*, Zenodo, doi: [10.5281/zenodo.10026684](https://doi.org/10.5281/zenodo.10026684)
- Johnson, B. D., Leja, J., Conroy, C., & Speagle, J. S. 2021, *ApJS*, 254, 22, doi: [10.3847/1538-4365/abef67](https://doi.org/10.3847/1538-4365/abef67)
- Kacprzak, G. G., Cooke, J., Churchill, C. W., Ryan-Weber, E. V., & Nielsen, N. M. 2013, *ApJL*, 777, L11, doi: [10.1088/2041-8205/777/1/L11](https://doi.org/10.1088/2041-8205/777/1/L11)
- Keerthi Vasan, G. C., Jones, T., Sanders, R. L., et al. 2023, *ApJ*, 959, 124, doi: [10.3847/1538-4357/acf462](https://doi.org/10.3847/1538-4357/acf462)
- Keerthi Vasan G., C., Jones, T., Shajib, A. J., et al. 2024, arXiv e-prints, arXiv:2402.00942, doi: [10.48550/arXiv.2402.00942](https://doi.org/10.48550/arXiv.2402.00942)
- Kennicutt, Robert C., J. 1998, *ARA&A*, 36, 189, doi: [10.1146/annurev.astro.36.1.189](https://doi.org/10.1146/annurev.astro.36.1.189)
- Kewley, L. J., & Dopita, M. A. 2002, *ApJS*, 142, 35, doi: [10.1086/341326](https://doi.org/10.1086/341326)
- Koester, B. P., Gladders, M. D., Hennawi, J. F., et al. 2010, *ApJL*, 723, L73, doi: [10.1088/2041-8205/723/1/L73](https://doi.org/10.1088/2041-8205/723/1/L73)
- Koposov, S., Speagle, J., Barbary, K., et al. 2023, *joshspeagle/dynesty: v2.1.3, v2.1.3*, Zenodo, doi: [10.5281/zenodo.8408702](https://doi.org/10.5281/zenodo.8408702)
- Kusakabe, H., Mauerhofer, V., Verhamme, A., et al. 2024, arXiv e-prints, arXiv:2406.04399, doi: [10.48550/arXiv.2406.04399](https://doi.org/10.48550/arXiv.2406.04399)
- Leclercq, F., Verhamme, A., Epinat, B., et al. 2022, *A&A*, 663, A11, doi: [10.1051/0004-6361/202142179](https://doi.org/10.1051/0004-6361/202142179)
- Lehner, N., Koppenhafer, C., O'Meara, J. M., et al. 2022, *ApJ*, 936, 156, doi: [10.3847/1538-4357/ac7400](https://doi.org/10.3847/1538-4357/ac7400)
- Leitherer, C., Tremonti, C. A., Heckman, T. M., & Calzetti, D. 2011, *AJ*, 141, 37, doi: [10.1088/0004-6256/141/2/37](https://doi.org/10.1088/0004-6256/141/2/37)
- Lodders, K. 2003, *ApJ*, 591, 1220, doi: [10.1086/375492](https://doi.org/10.1086/375492)
- Lopez, S., Tejos, N., Ledoux, C., et al. 2018, *Nature*, 554, 493, doi: [10.1038/nature25436](https://doi.org/10.1038/nature25436)
- Lopez, S., Tejos, N., Barrientos, L. F., et al. 2020, *MNRAS*, 491, 4442, doi: [10.1093/mnras/stz3183](https://doi.org/10.1093/mnras/stz3183)
- Lopez, S., Afruni, A., Zamora, D., et al. 2024, *A&A*, 691, A356, doi: [10.1051/0004-6361/202451200](https://doi.org/10.1051/0004-6361/202451200)
- Ma, X., Hopkins, P. F., Faucher-Giguère, C.-A., et al. 2016, *MNRAS*, 456, 2140, doi: [10.1093/mnras/stv2659](https://doi.org/10.1093/mnras/stv2659)
- Martin, C. L., Ho, S. H., Kacprzak, G. G., & Churchill, C. W. 2019, *ApJ*, 878, 84, doi: [10.3847/1538-4357/ab18ac](https://doi.org/10.3847/1538-4357/ab18ac)
- Morrissey, P., Matuszewski, M., Martin, D. C., et al. 2018, *ApJ*, 864, 93, doi: [10.3847/1538-4357/aad597](https://doi.org/10.3847/1538-4357/aad597)
- Morton, D. C. 2003, *ApJS*, 149, 205, doi: [10.1086/377639](https://doi.org/10.1086/377639)
- Muratov, A. L., Kereš, D., Faucher-Giguère, C.-A., et al. 2017, *MNRAS*, 468, 4170, doi: [10.1093/mnras/stx667](https://doi.org/10.1093/mnras/stx667)
- Naab, T., & Ostriker, J. P. 2017, *ARA&A*, 55, 59, doi: [10.1146/annurev-astro-081913-040019](https://doi.org/10.1146/annurev-astro-081913-040019)
- Neill, D., Matuszewski, M., Martin, C., Brodheim, M., & Rizzi, L. 2023, *KCWI.DRP: Keck Cosmic Web Imager Data Reduction Pipeline in Python*, Astrophysics Source Code Library, record ascl:2301.019
- Nielsen, N. M., Churchill, C. W., & Kacprzak, G. G. 2013a, *ApJ*, 776, 115, doi: [10.1088/0004-637X/776/2/115](https://doi.org/10.1088/0004-637X/776/2/115)
- Nielsen, N. M., Churchill, C. W., Kacprzak, G. G., & Murphy, M. T. 2013b, *ApJ*, 776, 114, doi: [10.1088/0004-637X/776/2/114](https://doi.org/10.1088/0004-637X/776/2/114)

- O'Meara, J., Prochaska, J. X., & Bordoloi, R. 2022, pypeit/kcwitools: v0.1.0, v0.1.0, Zenodo, doi: [10.5281/zenodo.6079396](https://doi.org/10.5281/zenodo.6079396)
- Oppenheimer, B. D., & Davé, R. 2006, MNRAS, 373, 1265, doi: [10.1111/j.1365-2966.2006.10989.x](https://doi.org/10.1111/j.1365-2966.2006.10989.x)
- Osterbrock, D. E., & Ferland, G. J. 2006, Astrophysics of gaseous nebulae and active galactic nuclei (University Science Books, Sausalito, CA)
- Pagel, B. E. J., Edmunds, M. G., Blackwell, D. E., Chun, M. S., & Smith, G. 1979, MNRAS, 189, 95, doi: [10.1093/mnras/189.1.95](https://doi.org/10.1093/mnras/189.1.95)
- Peeples, M. S., Werk, J. K., Tumlinson, J., et al. 2014, ApJ, 786, 54, doi: [10.1088/0004-637X/786/1/54](https://doi.org/10.1088/0004-637X/786/1/54)
- Péroux, C., & Howk, J. C. 2020, ARA&A, 58, 363, doi: [10.1146/annurev-astro-021820-120014](https://doi.org/10.1146/annurev-astro-021820-120014)
- Perrotta, S., Coil, A. L., Rupke, D. S. N., et al. 2024, arXiv e-prints, arXiv:2409.10013, doi: [10.48550/arXiv.2409.10013](https://doi.org/10.48550/arXiv.2409.10013)
- Pillepich, A., Springel, V., Nelson, D., et al. 2018, MNRAS, 473, 4077, doi: [10.1093/mnras/stx2656](https://doi.org/10.1093/mnras/stx2656)
- Rauch, M., Sargent, W. L. W., Barlow, T. A., & Simcoe, R. A. 2002, ApJ, 576, 45, doi: [10.1086/341267](https://doi.org/10.1086/341267)
- Reichardt Chu, B., Fisher, D. B., Nielsen, N. M., et al. 2022, MNRAS, 511, 5782, doi: [10.1093/mnras/stac420](https://doi.org/10.1093/mnras/stac420)
- Rigby, J. R., Bayliss, M. B., Sharon, K., et al. 2018a, AJ, 155, 104, doi: [10.3847/1538-3881/aaa2ff](https://doi.org/10.3847/1538-3881/aaa2ff)
- Rigby, J. R., Bayliss, M. B., Chisholm, J., et al. 2018b, ApJ, 853, 87, doi: [10.3847/1538-4357/aaa2fc](https://doi.org/10.3847/1538-4357/aaa2fc)
- Rubin, K. H. R., Prochaska, J. X., Koo, D. C., et al. 2014, ApJ, 794, 156, doi: [10.1088/0004-637X/794/2/156](https://doi.org/10.1088/0004-637X/794/2/156)
- Rubin, K. H. R., Prochaska, J. X., Koo, D. C., Phillips, A. C., & Weiner, B. J. 2010a, ApJ, 712, 574, doi: [10.1088/0004-637X/712/1/574](https://doi.org/10.1088/0004-637X/712/1/574)
- Rubin, K. H. R., Weiner, B. J., Koo, D. C., et al. 2010b, ApJ, 719, 1503, doi: [10.1088/0004-637X/719/2/1503](https://doi.org/10.1088/0004-637X/719/2/1503)
- Rubin, K. H. R., O'Meara, J. M., Cooksey, K. L., et al. 2018, ApJ, 859, 146, doi: [10.3847/1538-4357/aaaeb7](https://doi.org/10.3847/1538-4357/aaaeb7)
- Rudie, G. C., Steidel, C. C., Trainor, R. F., et al. 2012, ApJ, 750, 67, doi: [10.1088/0004-637X/750/1/67](https://doi.org/10.1088/0004-637X/750/1/67)
- Rupke, D. 2018, Galaxies, 6, 138, doi: [10.3390/galaxies6040138](https://doi.org/10.3390/galaxies6040138)
- Rupke, D. S., Veilleux, S., & Sanders, D. B. 2005, ApJS, 160, 87, doi: [10.1086/432886](https://doi.org/10.1086/432886)
- Rupke, D. S. N., Coil, A., Geach, J. E., et al. 2019, Nature, 574, 643, doi: [10.1038/s41586-019-1686-1](https://doi.org/10.1038/s41586-019-1686-1)
- Sato, T., Martin, C. L., Noeske, K. G., Koo, D. C., & Lotz, J. M. 2009, ApJ, 696, 214, doi: [10.1088/0004-637X/696/1/214](https://doi.org/10.1088/0004-637X/696/1/214)
- Schaye, J., Crain, R. A., Bower, R. G., et al. 2015, MNRAS, 446, 521, doi: [10.1093/mnras/stu2058](https://doi.org/10.1093/mnras/stu2058)
- Shaban, A., Bordoloi, R., Chisholm, J., et al. 2022, ApJ, 936, 77, doi: [10.3847/1538-4357/ac7c65](https://doi.org/10.3847/1538-4357/ac7c65)
- . 2023, MNRAS, 526, 6297, doi: [10.1093/mnras/stad3004](https://doi.org/10.1093/mnras/stad3004)
- Sharon, K., Bayliss, M. B., Dahle, H., et al. 2020, ApJS, 247, 12, doi: [10.3847/1538-4365/ab5f13](https://doi.org/10.3847/1538-4365/ab5f13)
- Somerville, R. S., & Davé, R. 2015, ARA&A, 53, 51, doi: [10.1146/annurev-astro-082812-140951](https://doi.org/10.1146/annurev-astro-082812-140951)
- Somerville, R. S., Hopkins, P. F., Cox, T. J., Robertson, B. E., & Hernquist, L. 2008, MNRAS, 391, 481, doi: [10.1111/j.1365-2966.2008.13805.x](https://doi.org/10.1111/j.1365-2966.2008.13805.x)
- Soto, K. T., Lilly, S. J., Bacon, R., Richard, J., & Conseil, S. 2016, MNRAS, 458, 3210, doi: [10.1093/mnras/stw474](https://doi.org/10.1093/mnras/stw474)
- Speagle, J. S. 2020, MNRAS, 493, 3132, doi: [10.1093/mnras/staa278](https://doi.org/10.1093/mnras/staa278)
- Spilker, J. S., Bezanson, R., Weiner, B. J., Whitaker, K. E., & Williams, C. C. 2019, ApJ, 883, 81, doi: [10.3847/1538-4357/ab3804](https://doi.org/10.3847/1538-4357/ab3804)
- Stewart, K. R., Brooks, A. M., Bullock, James S. aFIXnd Maller, A. H., et al. 2013, ApJ, 769, 74, doi: [10.1088/0004-637X/769/1/74](https://doi.org/10.1088/0004-637X/769/1/74)
- Strickland, D. K., & Heckman, T. M. 2009, ApJ, 697, 2030, doi: [10.1088/0004-637X/697/2/2030](https://doi.org/10.1088/0004-637X/697/2/2030)
- Tejos, N., López, S., Ledoux, C., et al. 2021, MNRAS, 507, 663, doi: [10.1093/mnras/stab2147](https://doi.org/10.1093/mnras/stab2147)
- Thompson, T. A., & Heckman, T. M. 2024, Annual Review of Astronomy and Astrophysics, 62
- Thompson, T. A., Quataert, E., Zhang, D., & Weinberg, D. H. 2016, MNRAS, 455, 1830, doi: [10.1093/mnras/stv2428](https://doi.org/10.1093/mnras/stv2428)
- Tonry, J. L., Stubbs, C. W., Lykke, K. R., et al. 2012, ApJ, 750, 99, doi: [10.1088/0004-637X/750/2/99](https://doi.org/10.1088/0004-637X/750/2/99)
- Tremonti, C. A., Heckman, T. M., Kauffmann, G., et al. 2004, ApJ, 613, 898, doi: [10.1086/423264](https://doi.org/10.1086/423264)
- Tumlinson, J., Peeples, M. S., & Werk, J. K. 2017, ARA&A, 55, 389, doi: [10.1146/annurev-astro-091916-055240](https://doi.org/10.1146/annurev-astro-091916-055240)
- Veilleux, S., Cecil, G., & Bland-Hawthorn, J. 2005, ARA&A, 43, 769, doi: [10.1146/annurev.astro.43.072103.150610](https://doi.org/10.1146/annurev.astro.43.072103.150610)
- Veilleux, S., Maiolino, R., Bolatto, A. D., & Aalto, S. 2020, A&A Rv, 28, 2, doi: [10.1007/s00159-019-0121-9](https://doi.org/10.1007/s00159-019-0121-9)
- Vogelsberger, M., Marinacci, F., Torrey, P., & Puchwein, E. 2020, Nature Reviews Physics, 2, 42, doi: [10.1038/s42254-019-0127-2](https://doi.org/10.1038/s42254-019-0127-2)
- Vogelsberger, M., Genel, S., Springel, V., et al. 2014, MNRAS, 444, 1518, doi: [10.1093/mnras/stu1536](https://doi.org/10.1093/mnras/stu1536)
- Weilbacher, P. M., Streicher, O., & Palsa, R. 2016, MUSE-DRP: MUSE Data Reduction Pipeline, Astrophysics Source Code Library, record ascl:1610.004

- Weilbacher, P. M., Palsa, R., Streicher, O., et al. 2020, *A&A*, 641, A28, doi: [10.1051/0004-6361/202037855](https://doi.org/10.1051/0004-6361/202037855)
- Werk, J. K., Prochaska, J. X., Tumlinson, J., et al. 2014, *ApJ*, 792, 8, doi: [10.1088/0004-637X/792/1/8](https://doi.org/10.1088/0004-637X/792/1/8)
- Xu, X., Heckman, T., Henry, A., et al. 2022, *ApJ*, 933, 222, doi: [10.3847/1538-4357/ac6d56](https://doi.org/10.3847/1538-4357/ac6d56)
- Xu, Y., Ouchi, M., Nakajima, K., et al. 2023, arXiv e-prints, arXiv:2310.06614, doi: [10.48550/arXiv.2310.06614](https://doi.org/10.48550/arXiv.2310.06614)
- Zabl, J., Bouché, N. F., Wisotzki, L., et al. 2021, *MNRAS*, doi: [10.1093/mnras/stab2165](https://doi.org/10.1093/mnras/stab2165)
- Zaritsky, D., Kennicutt, Robert C., J., & Huchra, J. P. 1994, *ApJ*, 420, 87, doi: [10.1086/173544](https://doi.org/10.1086/173544)